Soil Moisture Retrieval in Slow-Moving Landslide Region Using SAOCOM L-Band: A Radiative Transfer Model Approach

Divyeshkumar Rana, *Student Member, IEEE*, Raphael Quast, Wolfgang Wagner, *Senior Member, IEEE*, Paolo Mazzanti, and Francesca Bozzano

***Abstract*—Radiative transfer models have been extensively applied in soil moisture studies; however, their application to L-band synthetic aperture radar (SAR) data has not been fully explored. This research introduces a comprehensive approach for soil moisture retrieval using SAOCOM L-band SAR dual-polarization data (VV–VH). The novel bistatic radiative transfer modeling framework (RT1) is used, validated previously with Sentinel-1 C-band SAR and advanced scatterometer (ASCAT) data. For the first time, the RT1 model is applied to SAOCOM L-band data over the Petacciato landslide area in Italy, covering the period from January 2021 to December 2023. A statistical comparison of soil moisture estimates derived from L-band SAR data ($\lambda = 23$ cm) is conducted, with the model's performance evaluated against multiple regional-scale soil moisture datasets, including ASCAT, ERA-5 Land, and soil moisture active passive. Validation is performed using soil moisture time series and advanced statistical methods. The study incorporates the antecedent precipitation index (API), calculated from precipitation in the days leading up to an event, as an indicator of soil moisture, helping assess retained moisture from prior rainfall. The proposed methodology exhibits high accuracy, as evidenced by a strong correlation ($r \geq 0.67$, RMSE $= 0.0936$ m^3/m^3, MSE $= 0.088$ m^3/m^3, and Bias $= -0.0603$ m^3/m^3) between the RT1 soil moisture retrieval and reference datasets, such as ASCAT data. This approach provides a reliable tool for continuous soil moisture monitoring in landslide-prone regions, with SAOCOM L-band SAR and radiative transfer modeling enhancing retrieval in complex and agricultural terrains for improved landslide monitoring.**

***Index Terms*—Antecedent precipitation index (API), bistatic radiative transfer model (RT1), mass movement, microwave, radiative transfer, SAOCOM L-band, soil moisture, synthetic aperture radar (SAR), vegetation.**

Received 2 December 2024; revised 29 January 2025, 16 April 2025, 27 May 2025, and 17 June 2025; accepted 18 June 2025. Date of publication 20 June 2025; date of current version 9 July 2025. *(Corresponding author: Divyeshkumar Rana.)*

Divyeshkumar Rana, Paolo Mazzanti, and Francesca Bozzano are with the Department of Earth Sciences, Sapienza University of Rome, 00185 Roma, Italy (e-mail: divyeshkumar.rana@uniroma1.it; paolo.mazzanti@uniroma1.it; francesca.bozzano@uniroma1.it).

Raphael Quast is with GeoSphere Austria, 1030, Vienna, Austria, and also with the Department of Geodesy and Geoinformation, 1040 TU Wien, Vienna, Austria (e-mail: raphael.quast@geo.tuwien.ac.at).

Wolfgang Wagner is with the Department of Geodesy and Geoinformation, TU Wien, 1030, Vienna, Austria (e-mail: wolfgang.wagner@geo.tuwien.ac.at).

Digital Object Identifier 10.1109/JSTARS.2025.3581934

Nomenclature

API	Antecedent precipitation index.
SAR	Synthetic aperture radar.
SMOS	Soil moisture and ocean salinity.
SMAP	Soil moisture active passive.
ASCAT	Advanced scatterometer.
MODIS	Moderate resolution imaging spectroradiometer.
WCM	Water cloud model.
RT1	Bistatic radiative transfer model.
CHIRPS	Climate hazards group infrared precipitation with station data.
DEM	Digital elevation model.
RTC	Radiometric terrain correction.
ASI	Italian Space Agency.
ESA	European Space Agency.
SLC	Single-look complex.
NESZ	Noise equivalent sigma zero.
METOP	Meteorological operational.
GEM	Goddard earth model 6.
LAI	Leaf area index.
swl1	Volumetric soil water layer 1.
DN	Digital numbers.
ω	Single-scattering albedo.
τ	Vegetation optical depth.
σ^0	Backscatter coefficient or sigma nought.
BRDF	Bidirectional reflectance distribution function.
$\hat{p}$	Volume-scattering phase function.
RMSH	Root-mean-square height.
IEM	Integral equation model.
PDFs	Probability density functions.
MSE	Mean-squared error.
RMSE	Root-mean-square error.

I. Introduction

SOIL moisture is a critical parameter in the hydrological cycle, influencing numerous environmental processes, including weather patterns, vegetation growth, and the occurrence of natural disasters, such as floods and landslides [1], [2], [3], [4]. In the context of landslides, soil moisture is pivotal in triggering slope instability [5], [6]. Monitoring soil moisture is particularly important for slow-moving landslides, which are often

intensified by prolonged rainfall and seasonal wetting and drying cycles [7].

Assessing the relationship between soil moisture and landslides necessitates high spatial and temporal resolution measurements of surface soil moisture (SSM) in regions prone to landslides. Landslides represent significant hazards worldwide. Soil moisture plays a critical role in increasing landslide susceptibility by increasing soil weight, reducing cohesion, and decreasing interparticle friction—factors that contribute to soil destabilization, particularly on steep slopes. In addition, elevated pore pressure resulting from increased soil moisture reduces soil shear strength and density, thereby further compromising slope stability [8], [9]. Therefore, monitoring soil moisture dynamics, facilitated by SAR technology, is essential for landslide hazard assessment and developing strategies to manage moisture and mitigate ground deformation risks. Accurate soil moisture data enhances the prediction of hydrological responses to rainfall, facilitating the development of more effective early warning systems [10]. Slow-moving landslides, which advance at rates ranging from millimeters to meters per year [11], are typically triggered by precipitation and can be monitored over decades using remote sensing (RS) and ground-based methods [12], [13]. RS has revolutionized soil moisture monitoring, providing large-scale, continuous datasets crucial for assessing landslide risks [14]. Moreover, soil moisture estimation is essential for managing water resources, predicting crop yields, and mitigating climate change impacts [15]. Among these technologies, SAR is particularly promising due to its ability to penetrate cloud cover and provide data irrespective of weather conditions [16]. SAR systems operate at various wavelengths, such as C-band (e.g., Sentinel-1) and L-band (e.g., SAOCOM), offering distinct tradeoffs between penetration depth and sensitivity to surface roughness [17].

While coarse-resolution (10–50 km) soil moisture data derived from microwave radiometers and scatterometers—such as SMOS [18], SMAP [19], and ASCAT [20]—provide valuable insights for large-scale numerical weather prediction and climate models, these datasets fail to capture local-scale soil moisture variations. Numerous small-scale applications, including localized weather prediction, risk, and disaster management, as well as hydrological, forestry, and agricultural practices, require a spatial resolution below 1 km to adequately represent local conditions and meet the specific needs of end users [21].

This high spatial resolution can be achieved through SAR instruments, such as the C-band SAR onboard the ESA Copernicus Sentinel-1 satellite constellation (S1A, S1B, and their upcoming successors S1C and S1D). Among available SAR sensors, Sentinel-1 is particularly well-suited for soil moisture monitoring due to its excellent temporal coverage [22]. However, the Sentinel-1 dataset exhibits unique sampling and measurement characteristics that necessitate adaptations to existing retrieval strategies [23], [35], [39], [24], [25], [26], [27], [28]. However, their moderate wavelengths limit their capability to penetrate deeper soil layers, where subsurface moisture conditions are critical [29]. L-band SAR, with its longer wavelength, provides greater soil penetration and is less affected by vegetation, making it more suitable for monitoring soil moisture in complex terrains and vegetated areas [30], [31], [32].

In addition to SAR, other RS technologies, such as passive microwave sensors (e.g., SMAP) and optical sensors (e.g., Sentinel-2), have been employed for soil moisture estimation [33], [34]. Sentinel-1 SAR imagery enables the retrieval of SSM with high spatial (100 m) and temporal resolution. This study introduces two methodologies for estimating soil moisture using Sentinel-1 data in VV polarization, in combination with Sentinel-2 optical imagery to account for vegetation effects [35]. Ma et al. [36] highlighted the potential of fusing active and passive microwave measurements for robust global SSM mapping. This study leveraged this potential by integrating L-band SMAP and C-band ASCAT data, which observe the Earth at comparable spatial scales. This novel approach aimed to enhance SSM estimation accuracy and temporal resolution. Furthermore, integrating satellite-based soil moisture estimates with ground-based measurements and hydrological models has enhanced the accuracy of soil moisture data across diverse environments.

Merlin et al. [37] applied a disaggregation algorithm to data from the SMOS mission and the MODIS, generating soil moisture maps with a spatial resolution of 1 km. Similarly, Paloscia et al. [38] utilized machine learning techniques with data from the Copernicus Sentinel-1 SAR to produce soil moisture maps at comparable resolutions. Foucras et al. [39] integrated Sentinel-1 SAR, Sentinel-2 optical imagery, and MODIS data to achieve an enhanced spatial resolution of 500 m using a change detection approach.

Despite these advancements, significant challenges remain in accurately estimating soil moisture, particularly in complex terrains and densely vegetated areas. One key limitation of current SAR-based methods is their sensitivity to surface roughness and vegetation, which can introduce errors in soil moisture retrieval [16]. Higher frequency SAR, such as X-band, is especially affected by these factors, resulting in less accurate soil moisture estimates in densely vegetated or rough surface regions [21], [40].

Another challenge concerns the temporal resolution of SAR data. Although SAR provides valuable information on soil moisture, high-frequency observations are essential to capture rapid fluctuations in soil moisture conditions, particularly following precipitation events that may induce landslides [3], [41], [42]. The integration of SAR data with complementary sources, such as passive microwave sensors, presents a promising strategy for addressing temporal gaps in soil moisture observations. However, significant challenges persist in achieving effective harmonization of data across different sensor platforms [36].

The WCM also faces limitations in representing complex radar signal interactions with land surfaces, particularly in regions with significant topographic and vegetation complexities [43]. Advanced models are necessary to effectively address these complexities [44], [45].

Radiative transfer models have been widely utilized in soil moisture retrieval studies; however, their application to L-band SAR data remains largely underexplored. Previous research has predominantly focused on employing radiative transfer models with data from scatterometers (e.g., ASCAT) and Sentinel-1 C-band SAR [46], [47]. Despite its significant potential, the use of SAOCOM L-band SAR data, which provides deeper soil

penetration and greater sensitivity to soil moisture variations, has not been extensively investigated. This gap underscores the need for further research into integrating radiative transfer modeling with SAOCOM L-band SAR data for improved soil moisture retrieval.

The bistatic first-order radiative transfer model (RT1) framework, developed by Quast [48], [49], was employed to estimate soil moisture using SAOCOM L-band dual-polarimetric datasets (VV–VH) in the landslide-prone Adriatic coastal region of Petacciato. This analysis provides valuable insights into the region's soil moisture dynamics.

This study presents a novel application of the RT1 for soil moisture retrieval using dual-polarization (VV–VH) SAOCOM L-band SAR data. It represents the first known effort to apply RT1 with SAOCOM data at a regional scale for landslide monitoring, focusing on the complex terrain and vegetated conditions of the Petacciato region in Italy from January 2021 to December 2023. By leveraging the deeper soil penetration and enhanced dielectric sensitivity of L-band SAR, the study extends the applicability of RT1 beyond previous implementations, which were primarily limited to ASCAT scatterometer and Sentinel-1 C-band data.

The methodology incorporates multisensor validation using ASCAT, ERA5-Land, and SMAP datasets to assess the reliability of RT1-derived soil moisture estimates in the absence of in situ measurements. In addition, rainfall data from the CHIRPS are used to compute the API, a key hydrometeorological variable for assessing soil saturation and landslide triggering potential.

This study addresses the challenges of complex topography and vegetation cover, thereby enhancing the operational capacity of SAOCOM for geohazard applications and providing a scalable, transferable framework for soil moisture monitoring in landslide-prone areas. The rest of this article is organized as follows. Section II outlines the study area. Section III describes the datasets and methodology. Section IV presents the results. Section V discusses the findings in the context of related studies. Finally, Section VI concludes this article.

II. Study Area

Petacciato is situated in the northwestern part of the Molise region in central Italy, within the outermost section of the central-southern Apennine chain [refer to Fig. 1(b)]. The hilly terrain of the region, in combination with its coastal proximity, increases the vulnerability of specific areas to landslides, especially during episodes of intense rainfall or seismic events. The Petacciato landslide exhibits rotational-translational movements, with displacements reaching tens of centimeters during reactivation events. Notably, the landslide extends beyond the shoreline, illustrating its impact on both terrestrial and marine environments. Its failure mechanism has been extensively investigated through hydromechanical modeling, which incorporates critical factors such as rainfall infiltration and material instability [50].

Regions characterized by steep slopes, unconsolidated soils, and inadequate drainage systems are particularly susceptible to landslides. A substantial proportion of these events affect clastic soft units exposed along cliffs and coastal slopes, which are widespread across the Mediterranean region. These geological units consist of a regressive marine sequence composed of clay, sandstone, and conglomerates dating from the Early to Middle Pleistocene [refer to Fig. 1(c)]. The strata dip northeastward at angles ranging from 3° to 8°, closely corresponding to the slope's inclination. Overlying these clays are layers of sand and conglomerate, measuring between 70 and 100 m in thickness, forming a robust cap upon which the town of Petacciato is built. The local stratigraphy features lithologies varying from clay and clayey silts to sandy clay, sand, and gravel [51], [52].

The landslide-prone zone illustrated in Fig. 1(b) is among the largest in Europe, notable both for its extent and the level of hazard it presents. Covering approximately 17 square kilometers, this area is particularly significant for its susceptibility to landslides. Within this zone, a four-square-kilometer section is distinguished by a prominent, active landslide scarp. Historical records indicate that reactivations of the Petacciato landslide date back to 1909, with notable events resulting in severe damage to local infrastructure and the ancient village. The landslide's activity is characterized by retrogressive movements at the crown area and a prograding toe extending into the submerged nearshore environment [53].

The substantial scale of this landslide-prone area, combined with the active features it contains, underscores the pressing need for comprehensive research, continuous monitoring, and the implementation of effective mitigation strategies to address potential hazards [54].

III. Materials and Methods

A. Digital Elevation Model

The TINITALY DEM, a seamless DEM of Italy released in 2007, represents bare-Earth elevations and is classified as a DEM. It was constructed by integrating individual DEMs sourced from various Italian regions and is provided as a 10-m resolution grid in GeoTIFF format. The DEM utilizes the UTM WGS 84 zone 32 projection system [refer to Fig. 1(d)]. The maximum elevation observed within this dataset is 209 m. This high-resolution DEM is a critical resource for RTC in SAR imagery and for determining local incidence angles in soil moisture retrieval applications [55], [56].

Slope, a key topographic attribute derived from a DEM, refers to the rate of change in elevation over a specified distance. Typically expressed in degrees, the slope indicates the steepness or incline of the terrain. It is calculated by analyzing elevation differences between neighboring DEM pixels. A slope value of 0° represents flat terrain, while 90° corresponds to a vertical cliff [refer to Fig. 1(e)]. Within the landslide body, the slope angles range from 30° to 50° in the active landslide scarp. The average slope across the area varies between 15° and 30°, with some sections featuring vertical cliffs.

B. SAOCOM L-Band Data

SAR instruments capture high-resolution imagery regardless of cloud cover, time of day, or weather conditions and can operate across various wavelengths. This study utilized data

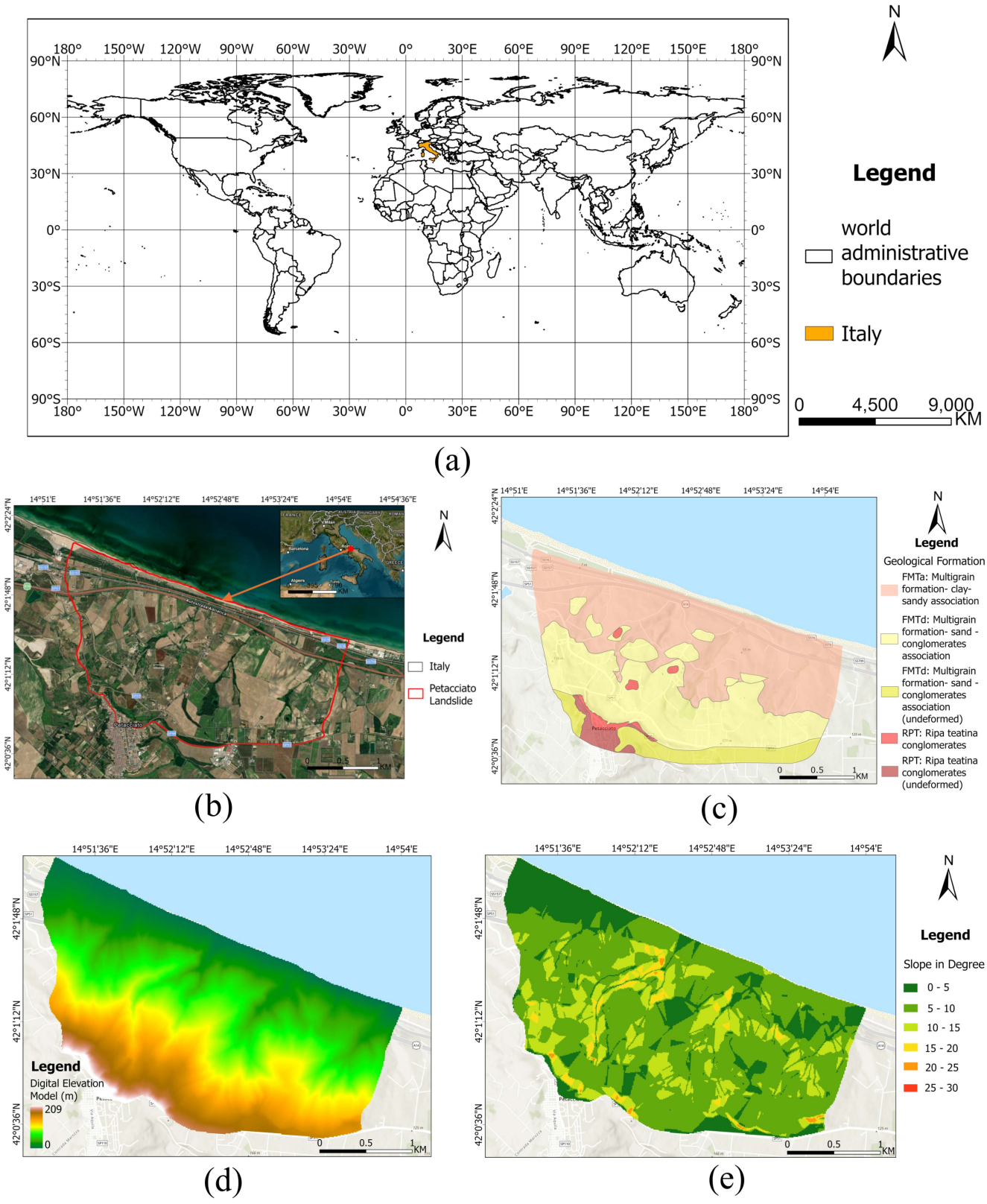

Fig. 1. (a) World map illustrating Italy country. (b) Study area map—Petacciato landslide (Red line represents the extent of the landslide area). (c) Geological formation map. (d) DEM map. (e) Slope map (in degrees) (Map Credits: World Topographic Map Esri, TomTom, Garmin, FAO, METI/NASA, USGS, CGIAR).

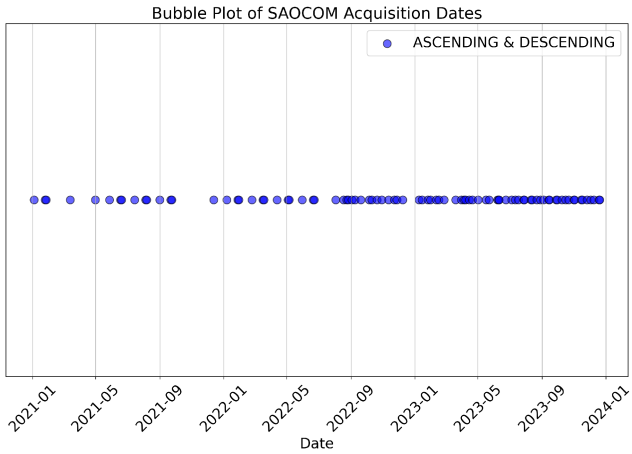

Fig. 2. SAOCOM acquisitions in ascending and descending orbit (total 90 images acquired).

TABLE I
TEMPORAL RESOLUTION AND SPATIAL RESAMPLING OF REFERENCE PRODUCTS

Product	Details
ASCAT	Data period: Jan 2021–Dec 2023 Temporal resolution: 0.4 d Spatial resampling: 6.25 km
ERA-5 Land	Data period: Jan 2021–Dec 2023 Temporal resolution: 1.0 d Spatial resampling: 9 km
SMAP-NSIDC	Data period: Jan 2021–Dec 2023 Temporal resolution: 0.12 d Spatial resampling: 9 km
CHIRPS	Data period: Jan 2021–Dec 2023 Temporal resolution: 5 d Spatial resampling: 5.5 km

from Argentina's SAOCOM L-band mission, distributed by the Italian Space Agency [57]. The mission consists of two Sun-synchronous satellites: SAOCOM-1 A, launched in 2018, and SAOCOM-1B, launched in 2020, providing a temporal resolution of 8 to 16 days. Soil moisture retrieval was conducted using data collected between January 2021 and December 2023 (refer to Fig. 2), processed by the RT1 package. The analysis employed SLC data in VV–VH polarization and STRIPMAP mode, with a resolution of 5 m in the range direction and 10 m in the azimuth direction. The processing workflow is thoroughly described in the methods section.

C. Reference Products

This section provides an overview of the reference products utilized in our analysis (refer to Table I for details).

1) ASCAT Data: It is a C-band active microwave RS instrument mounted on the meteorological operational satellite series. Although initially designed to measure wind speed and direction over oceans and not specifically intended for soil moisture monitoring, the instrument's characteristics—particularly its 5.7 cm wavelength, high radiometric accuracy, and multiple viewing capabilities—render it a valuable tool for soil moisture measurements [64].

The EUMETSAT HSAF ASCAT soil moisture product features a spatial resolution of 25 km and spatial sampling of 6.5 km, utilizing the WARP 5 Grid (sinusoidal DGG) with 82 nodes per swath row. It is referenced to the Goddard Earth Model 6 and is distributed by HSAF. The data are available as a time series in a binary format, with updates provided infrequently since 1 January 2007. The spatial coverage spans from 60°S to 80°N and 180°W to 180°E, with soil moisture values expressed as relative values, where 0 represents dry conditions and 100 indicates saturation. The soil moisture unit is converted from % saturation to m^3/m^3 for uniformity of the reference dataset [65].

2) ERA-5 Land Reanalysis Data: The ERA5-Land dataset is an enhanced version of the ERA5 climate reanalysis, offering a spatial resolution with a grid spacing of 9 km [58]. It provides comprehensive information on soil and vegetation variables at hourly intervals on a global scale. For this study, the following parameters were utilized.

a) *lai_lv (Parameter ID: 66): LAI, Low Vegetation [m^2/m^2]:* This parameter represents the surface area of one side of all the leaves within a specified land area for vegetation classified as "low," which includes crops, mixed farming, irrigated crops, short grass, tall grass, tundra, semidesert, bogs, marshes, evergreen shrubs, deciduous shrubs, and water-land mixtures. The data are utilized to simulate the seasonal impact on signal attenuation as the L-band propagates through the vegetation layer. For more information on the incorporation of LAI variability, please refer to Section IV.

b) *swvl1 (Parameter ID: 39): Volumetric Soil Water Layer 1 [m^3/m^3]:* This parameter quantifies the volume of water in soil layer 1, which extends from 0 to 7 cm in depth, with the surface level defined as 0 cm. The dataset serves as a reference for assessing the quality of the retrievals presented in Section IV.

3) SMAP Data: The SMAP Level-4 soil moisture product provides continuous data on surface and root-zone soil moisture, alongside variables such as surface meteorological forcing, soil temperature, evapotranspiration, and net radiation. During SMAP instrument outages, soil moisture estimates rely solely on land model simulations without the assimilation of SMAP brightness temperature data, as seen during outages in mid-2019 and late 2022. The product integrates SMAP L-band brightness temperature data from satellite passes into a land surface model gridded using the 9 km EASE-Grid 2.0 projection. In addition, SPL4SMGP provides 3-hourly geophysical data fields, transformed into geographic coordinates using the Geospatial Data Abstraction Library for integration with Google Earth Engine (GEE) [60].

The SMAP satellite soil moisture product is widely used for agriculture and water resource management [77]. Time-series SSM data acquired from GEE for the period between 1 January 2021, and 31 December 2023, is used as a reference dataset to evaluate the quality of retrieval from the RT1 algorithm.

4) CHIRPS Rainfall Data and API: CHIRPS is a 30+ year quasi-global rainfall data set. Spanning 50°S–50°N (and all longitudes), starting in 1981 to near-present, CHIRPS incorporates 0.05° resolution satellite imagery with in situ station data to create gridded rainfall time series for trend analysis and seasonal drought monitoring. As of 12 February 2015, version 2.0 of CHIRPS is complete and available to the public [66].

The API is commonly employed to estimate surface runoff based on recorded rainfall events, typically measured through rain gauges or other estimation techniques in watersheds that are either unmonitored or lack direct hydrological data, such as discharge records [80]. API is calculated by considering the precipitation recorded in the days preceding the event it refers to and can also serve as an indicator of soil moisture. The initial water content of the soil plays a critical role in shaping the runoff response, as dry soils react differently compared to moist or saturated soils. Although the underlying physical processes are complex, conceptually, this variation in response can be attributed to a reduction in the soil's infiltration capacity [81].

Kohler and Linsley [82] introduced the following equation for calculating the API

$$\text{API} = \sum_{t=-i}^{-1} P_t k^{-t} \tag{1}$$

where i denotes the number of antecedent days, k is a decay constant, often referred to as the recession coefficient, and P_t represents the precipitation on the day t. This model is also sometimes referred to as "retained rainfall" [83].

Equation (1) presents the recession coefficient as constant, which disagrees with the physical processes that vary at different temporal scales. The recession coefficient should consider water losses due to evapotranspiration or drainage. Here, the decay constant is set to 0.85. The decay constant, denoted as k, represents the rate at which the influence of previous precipitation on the API decreases over time. A value of 0.85 for k implies that 85% of the precipitation from the previous day is "retained" in the index for the following day, while 15% is "lost" or no longer considered influential. This indicates that the watershed or soil retains a significant portion of past precipitation, making it suitable for areas with moderate water infiltration, storage, or runoff. A lower value (e.g., 0.5) would indicate faster decay, meaning that past rainfall has a shorter-term influence, while a higher value (e.g., 0.95) would suggest slower decay, with precipitation having a more extended effect.

D. Methods

This study utilized time-series data from the SAOCOM *L*-band SAR datasets collected in 2021, 2022, and 2023. A total of 90 images from the SAOCOM *L*-Band dataset were processed and analyzed. The SLC data were obtained and preprocessed using SNAP software. The preprocessing steps included radiometric calibration, which converts pixel values from digital numbers to a standard geophysical measurement unit of radar backscatter; slant-range to ground-range conversion, which adjusts pixel geometry to a geographic projection for scientific analysis; and multilooking, which employs spatial averaging to reduce image speckle noise while converting the data to ground range, resulting in images with standardized pixel sizes and reduced resolution.

A refined Lee speckle filter (5×5) was then applied to effectively remove noise or speckles in the images without further compromising spatial resolution. Preprocessing SAR data to address geometric distortions, particularly in regions with significant topographic variation, necessitates a rigorous and systematic approach to ensure analytical accuracy. A central aspect of this preprocessing is RTC, which resolves both geometric and radiometric distortions. Geometric terrain correction, commonly referred to as geocoding, employs high-resolution DEMs to rectify pixel locations affected by terrain slopes and elevation changes, thereby ensuring precise alignment with geographic coordinates. In addition, radiometric terrain normalization addresses distortions arising from variations in incident angles and backscatter intensity by implementing pixel-specific corrections based on the DEM. Collectively, these procedures effectively mitigate geometric distortions and guarantee a consistent, accurate representation of SAR backscatter data, establishing RTC as an indispensable preprocessing method for studies involving complex terrain [84].

Spatial resolution: To mitigate noise and speckle effects, SAOCOM data were resampled to an effective spatial resolution of 500 m before soil moisture retrieval. Each 500 m $\times$ 500 m pixel encompasses a variety of soil and vegetation characteristics, providing spatially averaged parameters that represent the integrated radar response within the pixel. This resampling—from the native SAOCOM resolution of around 10 m to a 500 m scale—aims to improve the robustness of soil moisture retrieval by accounting for the complex SAR signal behavior observed at finer spatial scales at 10 m.

Temporal resolution: The SAOCOM constellation satellites (S1A and S1B) operate in a near-polar, sun-synchronous orbit with a temporal resolution of an 8- to 16-day repeat cycle. Data acquisition is nonuniform across ascending and descending passes. Subsequently, both ascending and descending geometries were combined.

Dynamic masking was applied to eliminate high backscatter responses from urban features and corner reflectors (≥ -2 dB) as well as low backscatter responses from water bodies (≤ -17 dB). This threshold was determined based on the spatial and temporal backscatter patterns of known water bodies across multiple SAOCOM acquisitions. This value reliably delineated both permanent and ephemeral water features with minimal misclassification. As SAOCOM's noise equivalent sigma zero typically ranges from –20 to –28 dB, the chosen threshold remains well above the sensor's detection limit, ensuring the validity of the observed low-backscatter responses. Please note that the RT1 model was implemented using VV polarization. The methodology is illustrated in Fig. 3. A comprehensive explanation of the RT1 model and its retrieval process is provided in the following section. Finally, validation was conducted through comparative analysis and advanced statistical techniques, as described in Section IV.

1) RT1 Model: The retrieval of soil moisture from radar data involves separating the measured backscatter sigma nought (σ^0)

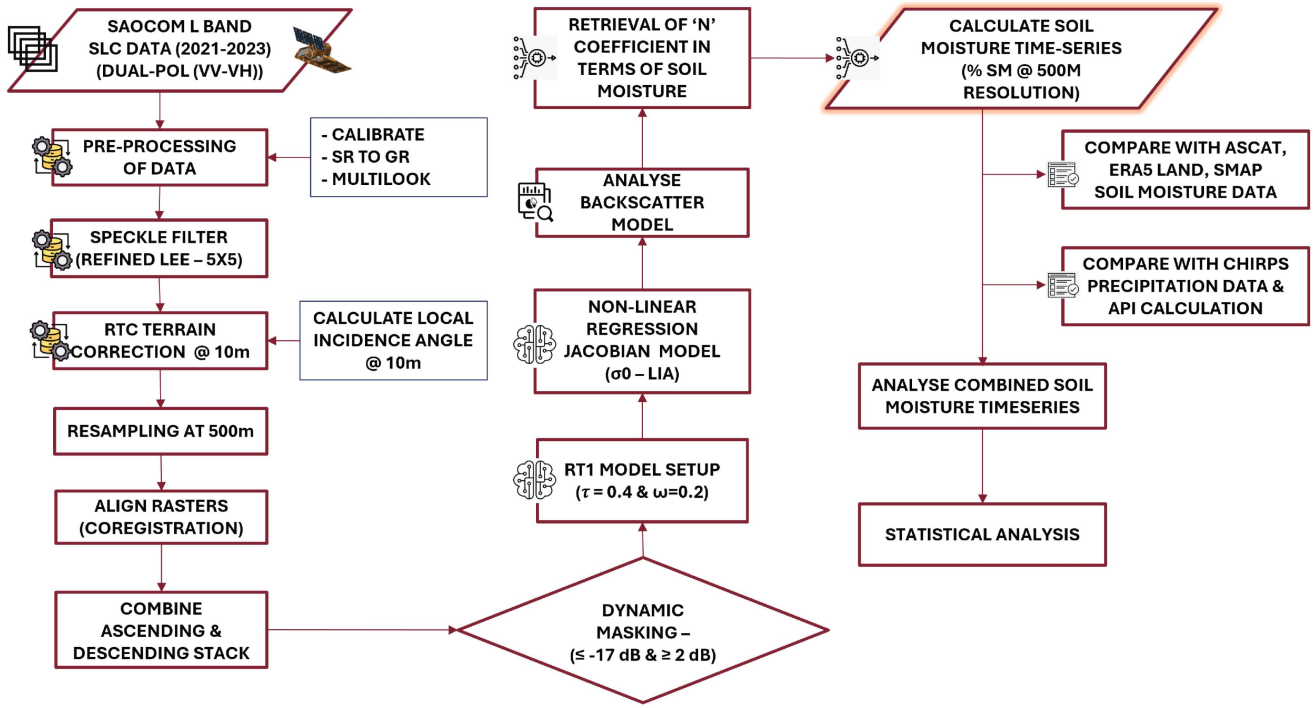

Fig. 3. Detailed methodology.

into contributions from soil and vegetation [17]. In this study, we utilize the RT1 model, a first-order radiative transfer model, combined with a nonlinear least squares optimization routine to achieve this separation [48].

The RT1 model describes the scattering response of a vegetation-covered surface using successive orders of scattering expansions of the radiative transfer equation. The approach applies to a rough surface covered by a sparse distribution of particulate media. A key assumption in this model is that radiation scattered more than once within the vegetation layer contributes minimally to the radar signal detected by the sensor. This simplification leads to *the optical depth* (τ) and *single-scattering albedo* (ω) model [17], where single-particle properties used in radiative transfer theory, such as the scattering coefficient (κ_s) and extinction coefficient (κ_{ex}), are encapsulated in the single-scattering albedo $\omega = \frac{\kappa_s}{\kappa_{\text{ex}}}$ and the optical depth $\tau = h\kappa_{\text{ex}}$. Here, h represents the height of the vegetation layer. The backscatter coefficient (σ^0) is represented as a power series in κ_s, where each term accounts for increasing scattering events

$$\begin{aligned}\sigma^0 = {} & \sigma^0_{\text{bare-soil}}\, e^{-\frac{2\tau}{\cos(\theta)}} \\ & + \sigma^0_{\text{vegetation}} \\ & + \sigma^0_{\mathcal{O}(\kappa_s)}\ \text{interactions} \\ & + \cdots . \end{aligned} \tag{2}$$

For bare soil, the response is described using the BRDF, which accounts for both the magnitude and directionality of the scattered radiation. For vegetation, the response is characterized by the volume-scattering phase function ($\hat{p}$), and the magnitude of the scattering response is governed by the ω [49]. The RT1 model is given by

$$\begin{aligned}\sigma^0 = {} & 4\pi\cos(\theta_0)\Bigg[f_{\text{bs}}\cos(\theta_0)\text{BRDF}(\ldots) \\ & + (1-f_{\text{bs}})\Bigg\{ e^{-\frac{2\tau}{\cos(\theta_0)}}\cos(\theta_0)\text{BRDF}(\ldots) \\ & + \frac{\omega}{2}\left(1-e^{-\frac{2\tau}{\cos(\theta_0)}}\right)\hat{p}(\ldots) \\ & + \sigma^0_{\text{int}}\Bigg\}\Bigg]. \end{aligned} \tag{3}$$

Here, f_{bs} represents the fraction of bare soil within the observed area, and $\sigma_{0,\text{int}}$ denotes all first-order interaction contributions, which are represented as half-space integrals over the product of $\hat{p}$ and the BRDF.

To fully specify the RT1 model, both $\hat{p}$ and BRDF, as well as effective vegetation parameters τ and ω, need to be parameterized. These parameters must be related to biophysical variables such as soil moisture, vegetation water content, and roughness. The complexity of these parameterizations must be balanced to ensure a physically meaningful representation of the scene while maintaining computational feasibility and avoiding issues of underdetermination in the retrieval procedures.

2) RT1 Model Parametrization: The following section provides a summary of the parameterization strategy employed in this study, along with a discussion of the implications and influencing factors that informed the selected parameterizations.

1) *Bare soil:* Many semiempirical bare soil scattering models exist in the literature that focus just on the parametrization

of the mono-static (e.g., backscattering) component of the scattered radiation via a combination of statistical roughness parameters such as correlation length (λ), RMSH, and Fresnel reflection coefficients [67], [68], [69], [73]. Nevertheless, to estimate the first-order interaction contributions (σ^0_{int}) in (2), the complete bistatic scattering characteristics must be parameterized.

In principle, electromagnetic scattering from a rough surface can be described with the help of the IEM [70] or its more recent successors like IEM2M [71] or AIEM [72]. While such models are very insightful for general scattering mechanisms, their use in parameter optimization, particularly for dynamic vegetation correction over large datasets, requires nonlinear regression that quickly becomes computationally prohibitive.

This study uses a scalable parametrization approach for soil scattering behavior modeling, which is a suitable method for big-data processing. This is achieved by employing a generalized Henyey–Greenstein function [47], defining the bistatic scattering behavior. It also contains a specular peak, normalized to the hemispherical reflectance at the nadir ($\theta_0 = 0$) and labeled as N. The width of the specular peak is controlled by a directionality parameter t, which varies from 0 for a Lambertian surface to 1 for a mirror-like surface, whereas the parameter a permits the introduction of anisotropy into the incidence-angle behavior.

This parametrization separates the parameters t and a, which govern the behavior in the incidence angle of the BRDF and are linked to soil roughness and texture, from the parameter N, which governs the overall scale of the scattered radiation and is connected to soil permittivity (ϵ), which at microwave wavelengths is highly dependent on the amount of moisture within the soil

$$\text{BRDF}(N,t,a) = \frac{N}{R_0(t,a)}\, HG(t,\tilde{\Theta}_a) \text{ with}$$

$$HG(t,\Theta) = \frac{1}{4\pi}\frac{1-t^2}{\left[1+t^2-2t\cos(\Theta)\right]^{3/2}}$$

$$\tilde{\Theta}_a = a\cos(\theta_0)\cos(\theta_s) - \sin(\theta_0)\sin(\theta_s)\cos(\phi_0-\phi_s)$$

$$R_0(t,a) = \frac{(1-t^2)}{2a^2t^2}\left[\frac{(1+t^2+at)-\sqrt{(1+t^2+2at)(1+t^2)}}{\sqrt{(1+t^2+2at)}}\right]. \tag{4}$$

Here, (θ_0,ϕ_0) and (θ_s,ϕ_s) represent the directions of the incident and scattered radiation, respectively. It is worth noting that this approach is not based directly on geometric, statistical roughness parameters in the form of λ and RMSH but provides a more general description of the bistatic scattering distribution caused by wave-particle interaction within the top few centimeters of soil. Hence, according to the general principle of retrieval, the effect of soil properties on the microwave backscattering coefficient $\sigma^0(\theta,\phi)$ is described by the scattering directionality parameter t, adapted within the retrieval process. This approach offers a solution that is both computationally effective and scalable for big-data applications.

2) *Vegetation:* The scattering and absorption of incoming radiation by vegetation are characterized by radiative transfer parameters such as the τ and ω. In addition, the angular scattering behavior of the vegetation is represented by a "volume scattering phase-function" ($\hat{p}$). Although theoretically, the shape of $\hat{p}$ can be estimated using statistical electrodynamics by approximating vegetation elements (like trunks and leaves) as simplified dielectric shapes [74], this study's dataset limits the possibility of retrieving a comprehensive set of parameters governing the incidence-angle dependency of the vegetation's contribution to $\sigma_0(\theta)$. Since only one incidence angle is available per measurement, both $\hat{p}$ and ω remain ambiguous parameters to the zero-order vegetation contribution described in (2). Disentangling these parameters would require either a detailed study of higher order interactions or bistatic measurements. However, such higher order corrections contribute minimally to the overall backscatter signal and remain sensitive to the parameterization of the BRDF. As a result, for monostatic measurements with limited incidence-angle variation, retrieving vegetation directionality parameters alongside (ω) is practically impossible. Therefore, an isotropic phase-function was assumed for $\hat{p}$

$$\hat{p}(\Theta) = \frac{1}{4\pi}. \tag{5}$$

It is important to note that this choice influences the magnitude of the estimated ω values since the zero-order vegetation contribution is proportional to $\omega^2\hat{p}(\dots)$. Any comparison of ω across studies must consider the associated choice of $\hat{p}$. To account for seasonal vegetation changes, the optical depth τ was modeled using the auxiliary LAI time series from the ERA5-Land dataset [58]. While the relationship between τ and LAI is typically complex and influenced by several physiological factors, parameterizing this relationship at a spatial resolution of 500 m remains challenging. Therefore, a simplified approach was adopted, assuming a homogeneous dynamic range [46]

$$\tau = \text{LAI} \rightarrow \text{scaled to } [0,1]. \tag{6}$$

This range avoids absorption saturation in the vegetation layer, recognizing that, at a 500 m resolution, parts of the pixel will likely have low or moderate vegetation cover. The use of auxiliary data inevitably introduces uncertainties that propagate to the final model parameters, complicating the retrieval process and potentially degrading soil moisture estimation performance. Although the ERA5-Land dataset has a spatial resolution of $\sim$9 km and reflects monthly climatology from the MODIS MOD12A2 LAI [58], [59], it provides a smooth, continuous time series for estimating seasonal vegetation dynamics. However, its spatial variability is insufficient to capture abrupt changes in σ_0 at finer resolutions like 500 m. Thus, the LAI

TABLE II
SUMMARY OF PARAMETER SPECIFICATIONS USED IN THE RESULTS

Param	Min	Max	Value
N	0.01	0.075	0.02
ω	0.01	0.50	0.20
t_s	0.01	0.50	0.15

dataset was harmonized to mitigate spatial representativeness issues, with the retrieved ω values capturing residual spatial variability within the RT1 parameterization.

3) Retrieval Procedure: The retrieval procedure employs a nonlinear least squares regression utilizing the trust-region reflective Levenberg–Marquardt algorithm [75], as implemented in the Python module `scipy.optimize` [76].

Given that the soil moisture state can vary significantly from one timestamp to the next, a distinct N value is optimized for each SAOCOM timestamp. According to [47], physical plausibility considerations—based on Kirchhoff's law and L-band emissivity measurements—suggest that $N < 0.1$. Consequently, the retrieval range for N is set between [0.01, 0.075], with an initial value of 0.02 The actual bare-soil scattering response $\sigma_{\text{bare-soil}}$ is influenced by both N and the directionality parameter t_s of the BRDF function [as defined in (4)]. This parameter is estimated for each pixel as a temporally constant value within the range of [0.01, 0.4], with a starting value of 0.2. The parameter t_s fully specifies the bistatic soil scattering directionality required for estimating first-order interaction contributions. It is important to note that, due to the mono-static nature of the measurements with a limited range of incidence angles, the bistatic part of the distribution should be regarded as a "best-guess" rather than a precise estimate, which could only be obtained with a true bistatic measurement setup.

The SAOCOM dataset is missing orbital data, possibly due to larger orbital tubes or other data acquisition challenges. Therefore, the permissible range for ω is set between [0.01, 0.5]. Given that ω is the primary parameter influencing the strength of the vegetation contribution, three different initial values (0.05, 0.20, and 0.4) were tested to evaluate the effect of different starting values on the parameter estimates. The summary of parameter specification is given in Table II.

IV. RESULTS

A. Soil Moisture Retrieval Performance

This section presents the results of the parameterization of the RT1 model applied to the time series from 1 January 2021 to 31 December 2023, using the retrieval start value ω, processed with and without the first-order interaction contribution. The soil moisture retrieval performance is discussed here. This analysis reveals a linear relationship between the nadir hemispherical reflectance (N) and the volumetric soil moisture in the topsoil layer. Please note that all comparative analyzes are based on the mean values of RT1 and reference datasets, including ASCAT, SMAP, ERA5, and API. Mean values are considered due to the unavailability of in situ soil moisture data, making comparisons with reference datasets more appropriate.

Fig. 4 presents the temporal evolution of VV-polarized backscatter (σ^0, in dB) acquired from ascending and descending SAOCOM orbits between 2021 and 2023. Fig. 5 illustrates the time series of soil moisture retrieved using the RT1 model from ascending and descending SAOCOM SAR orbits over the same period.

Fig. 6 presents a time series comparison of soil moisture data from multiple sources between January 2021 and December 2023. The left y-axis represents mean soil moisture levels in m^3/m^3 for the ASCAT, SMAP, and ERA5 datasets, while the right y-axis displays the mean scaled RT1-SM values in percentage. The ASCAT and SMAP datasets, depicted with dashed blue and orange lines, respectively, exhibit similar trends characterized by rapid fluctuations across seasons, particularly after precipitation events. In contrast, the ERA5 dataset, represented by a solid green line, demonstrates a more stable trend with reduced variability. The RT1-SM values, illustrated by red dots and scaled on the right y-axis, are compared with three reference datasets: ASCAT, SMAP, and ERA5. The comparison between the RT1-retrieved soil moisture and the reference datasets offers important insights into model behavior, performance, and seasonal dynamics. Notably, the RT1, ASCAT, and SMAP datasets exhibit consistent overall trends.

B. Impact of Vegetation on Soil Moisture Retrieval Accuracy

L-band ($\lambda = 23\,\text{cm}$) can penetrate sparse to moderate vegetation canopies, interacting with both the canopy and the underlying soil. In vegetated areas, the backscatter is influenced by both the canopy and the soil surface, with signal attenuation and scattering depending on factors such as vegetation type, density, moisture content, and the LAI. The LAI, defined as the ratio of leaf surface area to ground area (m^2/m^2), plays a critical role in soil moisture retrieval using the RT1 model. In such regions, LAI significantly impacts the scattering and absorption of microwave signals emitted or reflected by the soil surface. A higher LAI typically leads to increased canopy scattering and reduced signal penetration, complicating the accurate detection of soil moisture. In the RT1 model, vegetation parameters such as LAI are incorporated to correct for these effects, thereby enhancing the precision of soil moisture estimates.

Consequently, LAI is a critical parameter for evaluating RT1 soil moisture despite the ambiguity in its spatial resolution. It facilitates the differentiation between the contributions of vegetation and soil moisture. Refer to Fig. 7 for further illustration.

C. Relationship Between API and RT1 SM

The API reflects the cumulative effect of prior rainfall on soil moisture levels. The relationship between the API and RT1 soil moisture is a critical factor in understanding hydrological processes and soil moisture dynamics. An explanation of the API is provided in Section III. Fig. 8 illustrates the relationship between the API and RT1 soil moisture, revealing a significant delay in the time series. This delay suggests that precipitation

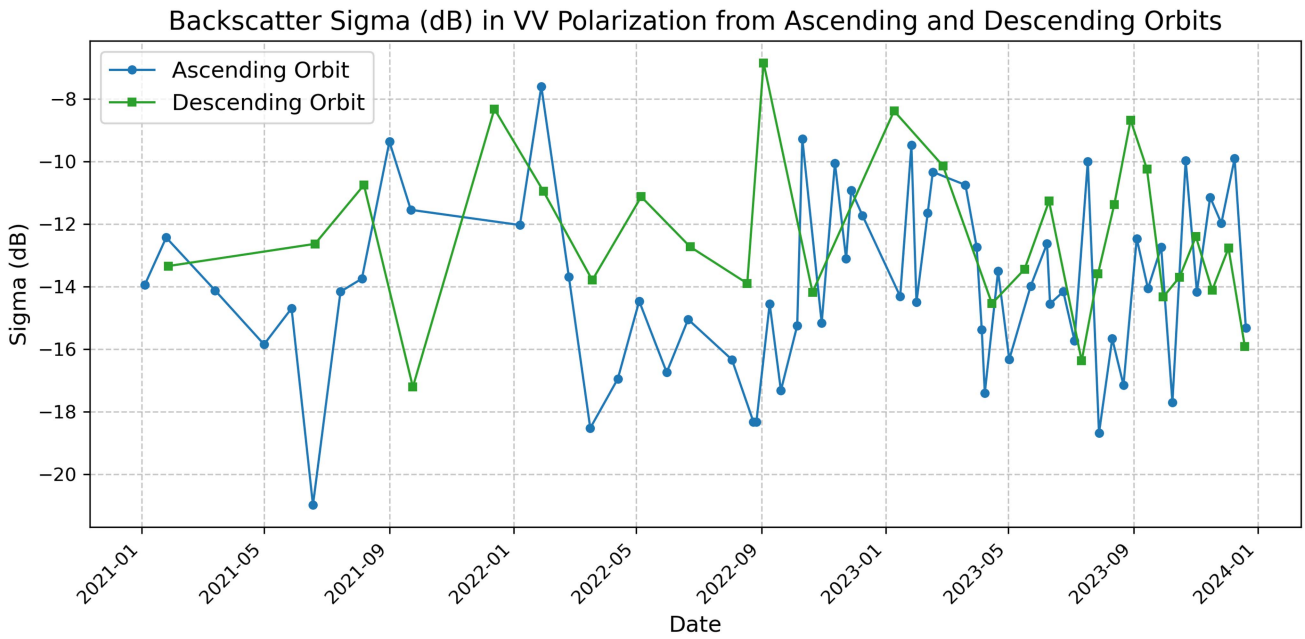

Fig. 4. Time series of VV-polarized backscatter sigma (dB) acquired from ascending (blue) and descending (green) SAOCOM orbital geometries. The plot illustrates temporal variations in SAR backscatter over the study area between 2021 and 2023 (Latitude: 42.017079, Longitude: 14.869953).

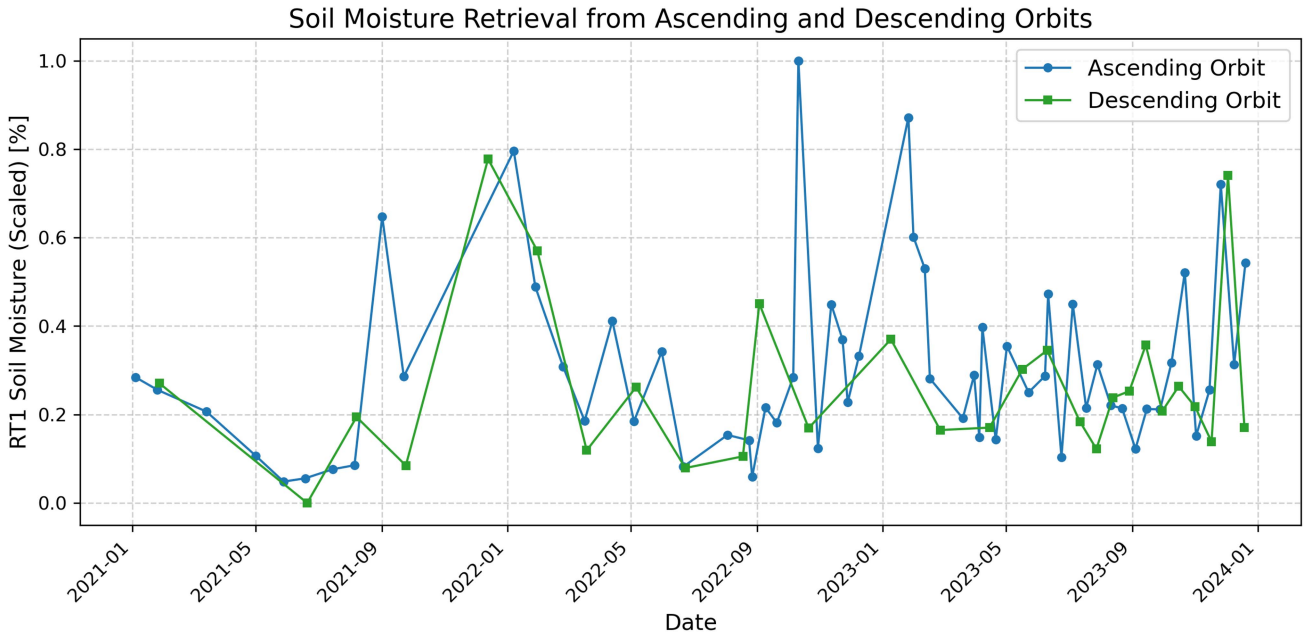

Fig. 5. Time series of mean-scaled soil moisture retrieval (RT1-SM) derived from ascending and descending SAOCOM orbits over the study area from 2021 to 2023. Ascending soil moisture is illustrated in blue color, and descending soil moisture is illustrated in green color.

does not directly lead to immediate changes in soil moisture levels due to the involvement of various complex processes, including percolation, runoff, and evapotranspiration.

From Fig. 9, the observed cross-correlation lags of 0 lag (corresponds to 5 days based on the temporal resolution) and 12 lag (corresponds to 60 days based on the temporal resolution) between the API and RT1 soil moisture. Please note that the effects may not be real due to the lack of physical evidence. Further details are discussed in Section V.

D. Statistical Intercomparison

Fig. 10 illustrates scatter plots demonstrating the correlations between RT1-SM and the reference datasets (swl1, ASCAT-SM, SMAP-SM, and API), each highlighted with a Pearson's correlation coefficient. For each pair, the scatter points represent individual data points, with a trendline indicating the overall direction of the relationship. Plots with higher Pearson's correlation values, such as RT1-SM versus ASCAT-SM ($r = 0.66$)

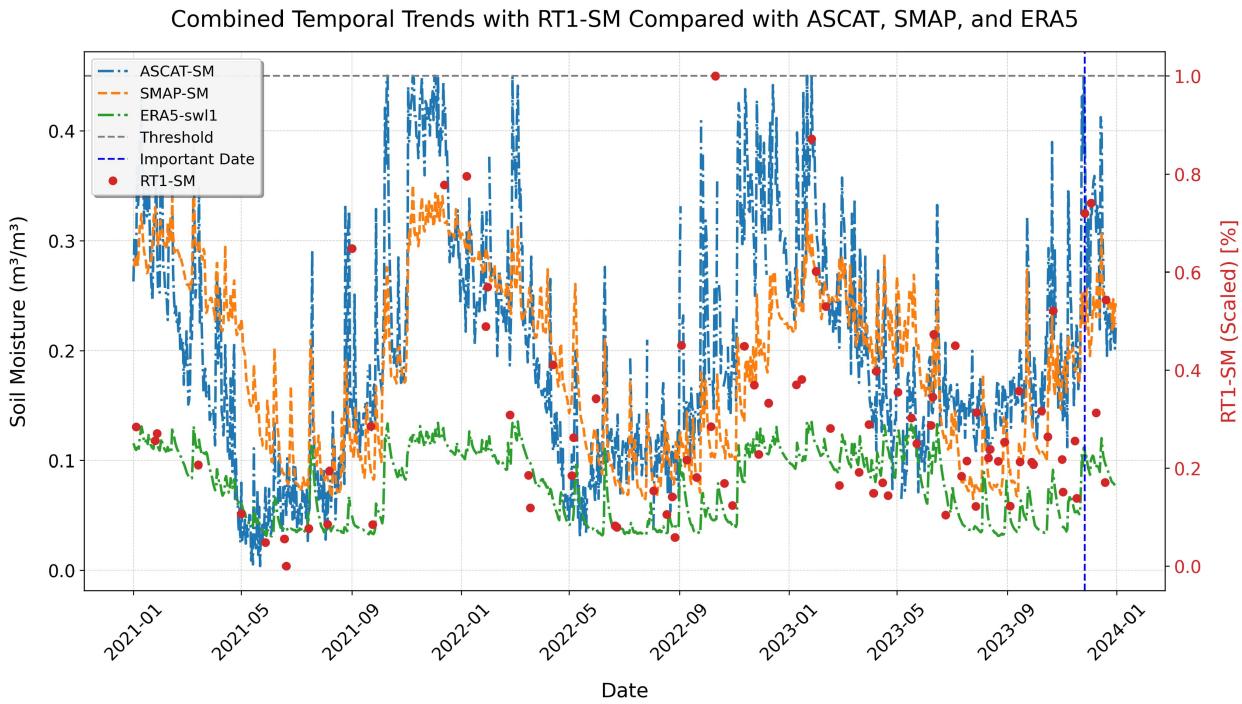

Fig. 6. Mean soil moisture time-series trends [2021–2023]: RT1-SM (dark red dots) compared to ASCAT (blue), SMAP (orange), and ERA5 (green). The gray line represents the maximum threshold for soil moisture, while the vertical blue line indicates the maximum soil moisture observed in the time series.

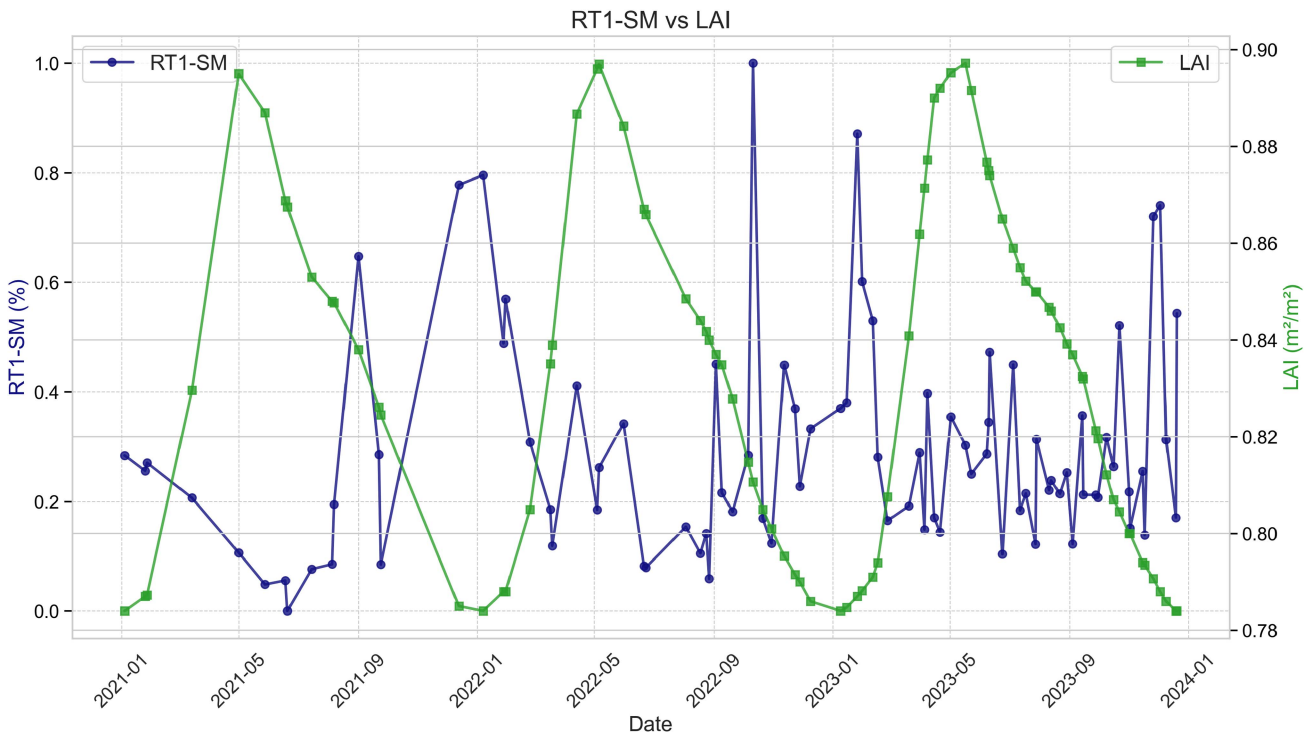

Fig. 7. Comparative time-series trends of RT1-SM (blue color) and LAI (green color) [2021–2023].

and SMAP-SM versus swl1 (ERA-5) ($r = 0.88$), demonstrate a clearer, more linear relationship. This suggests that these variables closely align in their representation of soil moisture dynamics. In contrast, plots with lower r values (e.g., RT1-SM versus SMAP-SM, $r = 0.43$) show more scatter around the trend line, suggesting that while the datasets are related, they capture different nuances of soil moisture.

Fig. 11 shows the Pearson's correlation heatmap, illustrating the strength and direction of linear relationships between RT1 retrieved soil moisture and reference datasets

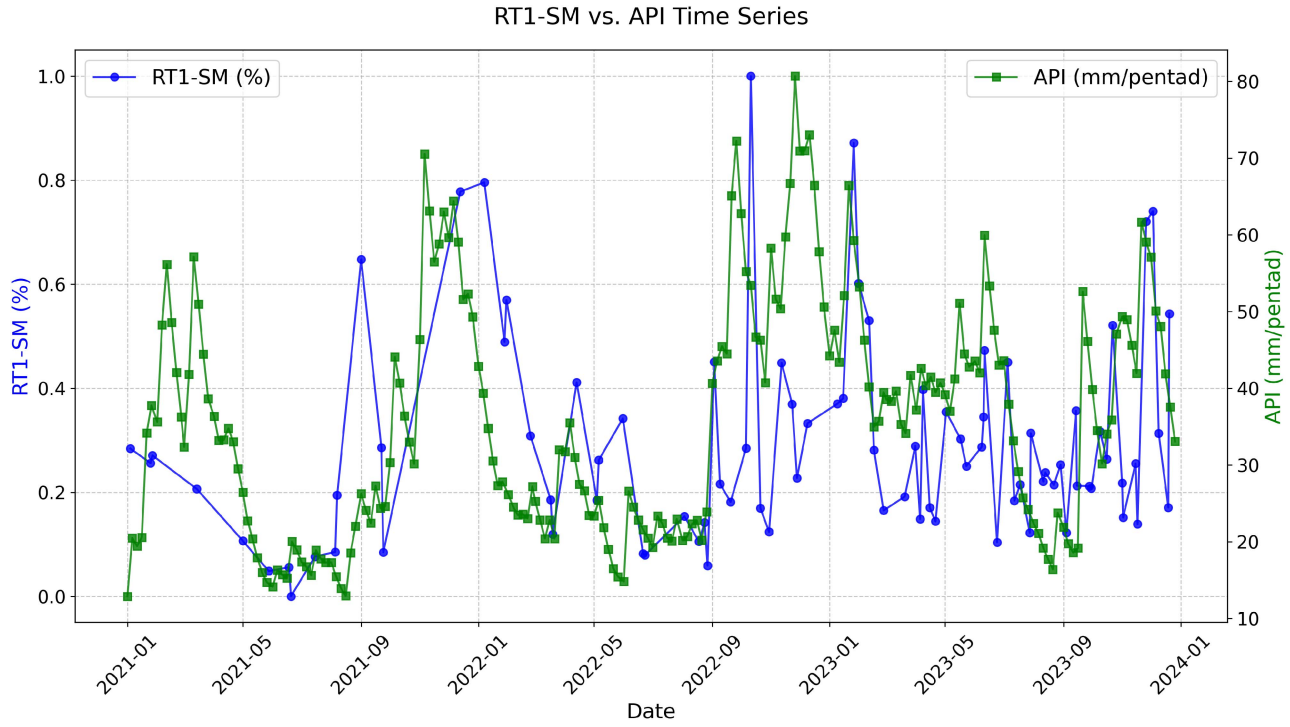

Fig. 8. Comparative time-series trends of RT1-SM (blue color) and API (green color) [2021–2023].

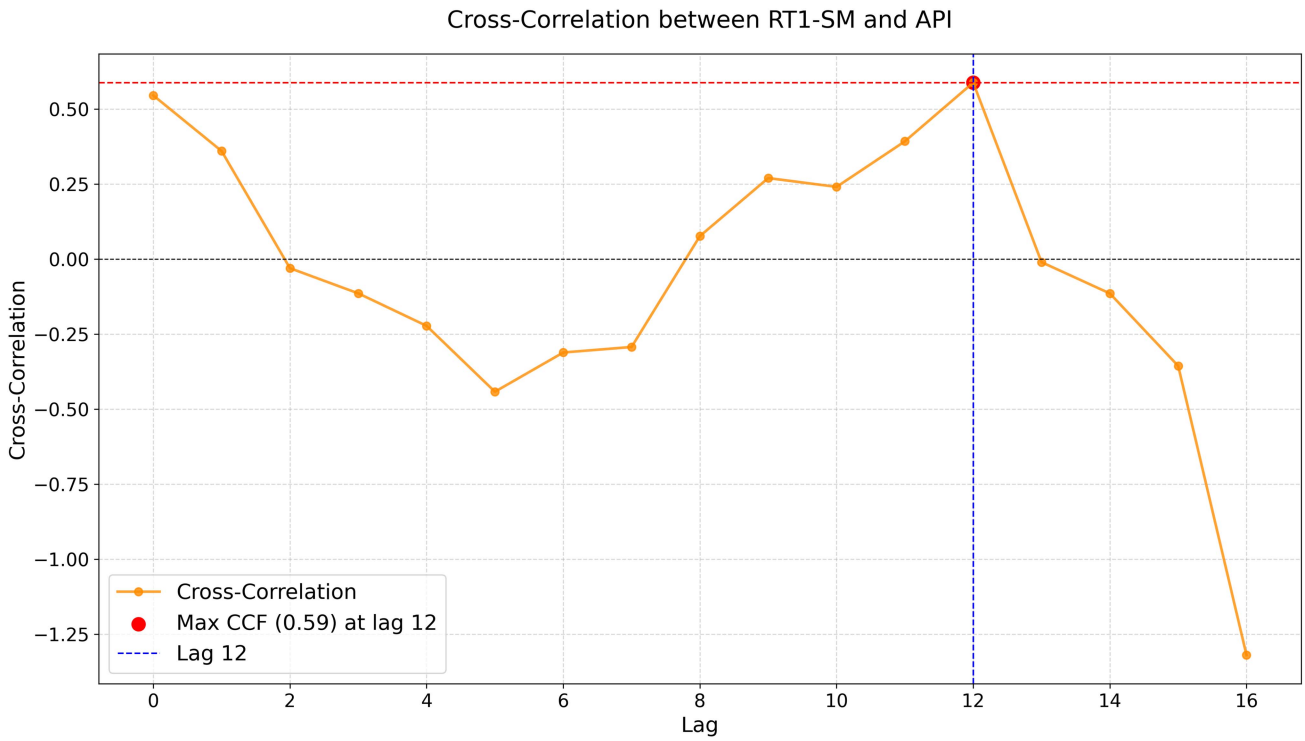

Fig. 9. Cross-correlation between RT1 soil moisture and API (highest peaks at lags 0 and 12).

(ASCAT-SM, SMAP-SM, swI1, and API). RT1 shows a strong positive correlation with ASCAT-SM, indicating that it closely tracks soil moisture patterns measured by ASCAT, likely responding similarly to changes in conditions despite potential differences in surface handling. The correlation with SMAP-SM is moderate, suggesting notable differences in measurement approaches, possibly due to variations in sensor technology or resolution. Similarly, RT1 has a moderate correlation with swI1, indicating some alignment but not fully capturing the same moisture dynamics. In contrast, RT1 exhibits a very strong correlation

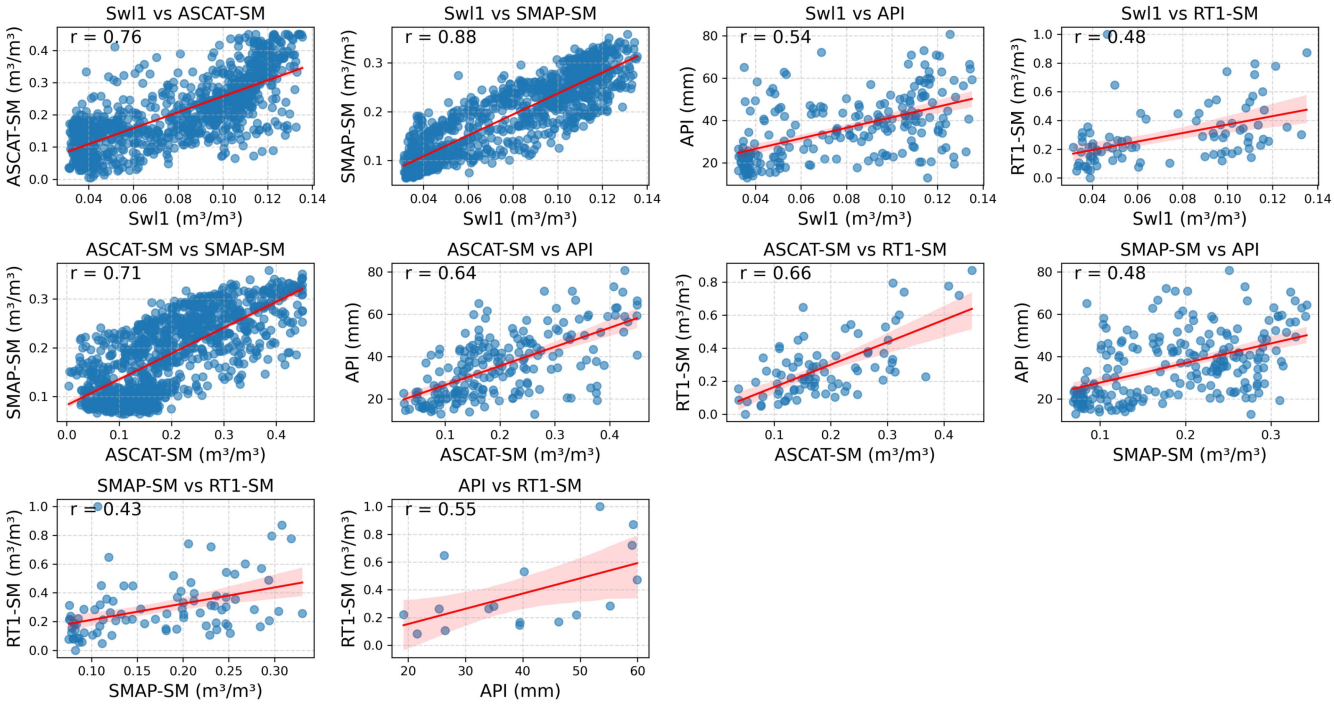

Fig. 10. Scatter plot along with Pearson's correlation coefficients of RT1-SM and reference dataset.

with the API, highlighting its responsiveness to recent rainfall and moisture accumulation, particularly during wetter periods. Overall, RT1 aligns well with ASCAT-SM and API, capturing short-term soil moisture fluctuations effectively while showing more moderate correlations with SMAP-SM and swI1, reflecting differences in how these datasets model soil moisture. RT1-SM correlates most strongly with ASCAT-SM ($r = 0.66$), indicating that these two datasets likely captured the same soil moisture dynamics.

1) Seasonality Decomposition: Seasonality decomposition is a statistical technique employed to analyze and elucidate the underlying components of a time series dataset by separating it into distinct elements: trend, seasonality, and residuals (or noise). This technique can be effectively implemented using the `seasonaldecompose` function from the Python package. The trend component represents the long-term progression of the series, indicating the general direction in which the data are moving over time. The seasonal component captures regular repeating patterns that occur at fixed intervals (e.g., weekly), reflecting the influence of cyclical factors such as seasonal cycles. The residual component comprises random fluctuations or irregularities that cannot be attributed to either trend or seasonal effects. By decomposing a time series into these components, analysts can gain a deeper understanding of the data's behavior and identify the underlying patterns that influence the observed values. Fig. 12 illustrates the seasonal variation of RT1-SM and ASCAT data. The ASCAT data were included in the analysis due to its high correlation with RT1-SM.

2) Soil Moisture Anomalies: Anomalies refer to deviations from the expected or average behavior of a dataset, highlighting unusual variations that can provide insights into underlying patterns or changes within the system being investigated. In our analysis, we employed a 30-day rolling mean to capture the underlying trends in the dataset while smoothing out short-term fluctuations. This approach allows for a clearer observation of the seasonal patterns and variations present in the data.

In the context of time series analysis, anomalies are calculated by subtracting the smoothed or seasonal component (such as the 30-day rolling mean) from the original values. This methodology allows researchers to identify significant deviations, whether positive or negative that may signal extraordinary events or fundamental shifts in the underlying process. By analyzing these anomalies, researchers can uncover trends, diagnose potential issues, and enhance their understanding of the dynamics influencing the dataset. Fig. 13 depicts the anomalies for the 30-day rolling period, calculated as the seasonality subtracted from the actual datasets.

3) Statistical Intercomparison of RT1-SM With SMAP, ASCAT, and ERA5 Using RMSE, and Bias: To evaluate the performance of RT1-retrieved soil moisture, originally expressed as % saturation, the values were converted to volumetric units ($\mathrm{m}^3/\mathrm{m}^3$) using

$$\theta_{\mathrm{RT1}} = f_s \times \phi \tag{7}$$

where θ_{RT1} is the volumetric soil moisture, f_s is the % saturation output of the RT1 model, and $\phi = 0.45$ was adopted based on values retrieved from the NASA GLDAS soil porosity database [88].

Pairwise statistical comparisons were performed between RT1-SM and other datasets (SMAP-SM, ASCAT-SM, ERA5-swl1) using the following metrics:

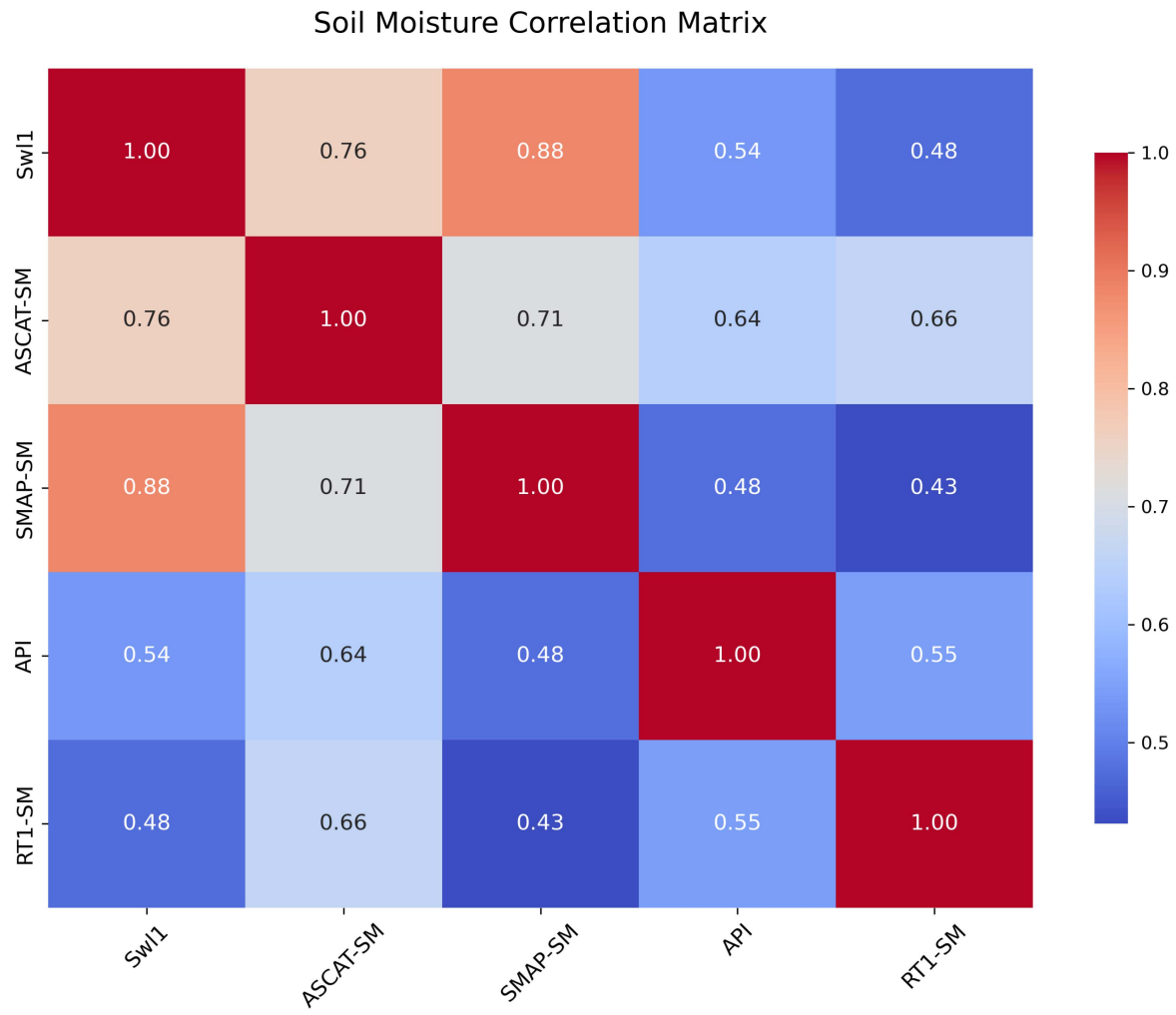

Fig. 11. Heatmap of Pearson's correlation coefficients between RT1-SM and reference dataset.

1) *Mean squared error (MSE)*:

$$\text{MSE} = \frac{1}{n}\sum_{i=1}^{n}(y_i - x_i)^2. \tag{8}$$

2) *RMSE*:

$$\text{RMSE} = \sqrt{\text{MSE}} = \sqrt{\frac{1}{n}\sum\nolimits_{i=1}^{n}(y_i - x_i)^2}. \tag{9}$$

3) *Bias*:

$$\text{Bias} = \frac{1}{n}\sum_{i=1}^{n}(y_i - x_i) \tag{10}$$

where

- x_i reference soil moisture value at time step i (e.g., SMAP-SM, ASCAT-SM, or ERA5-swl1);
- y_i corresponding RT1-derived soil moisture value;
- n total number of valid (nonmissing) paired observations.

To assess the agreement between RT1-derived soil moisture and reference datasets, three standard statistical metrics were employed. MSE quantifies the average of the squared differences between paired observations, capturing both the variance and systematic deviation between the datasets. RMSE, being the square root of MSE, retains the original units (m^3/m^3) and provides an interpretable measure of the overall error magnitude. The bias represents the average difference between the reference and target values, indicating whether the retrievals systematically overestimate or underestimate soil moisture. Together, these metrics offer a comprehensive evaluation of retrieval accuracy and consistency [87]. API was deliberately omitted from the evaluation to avoid inconsistencies arising from unit discrepancies.

Table III presents the summary of error metric results.

V. Discussion

This study constitutes the first regional-scale application of SAOCOM L-band SAR data for soil moisture retrieval using the RT1 model, specifically adapted for landslide-prone regions. By integrating dual-polarimetric L-band SAR observations within the RT1 framework, the research advances the operational utility of SAOCOM for landslide monitoring.

Fig. 4 presents the backscatter signal, which is influenced by soil moisture, vegetation water content, and surface roughness.

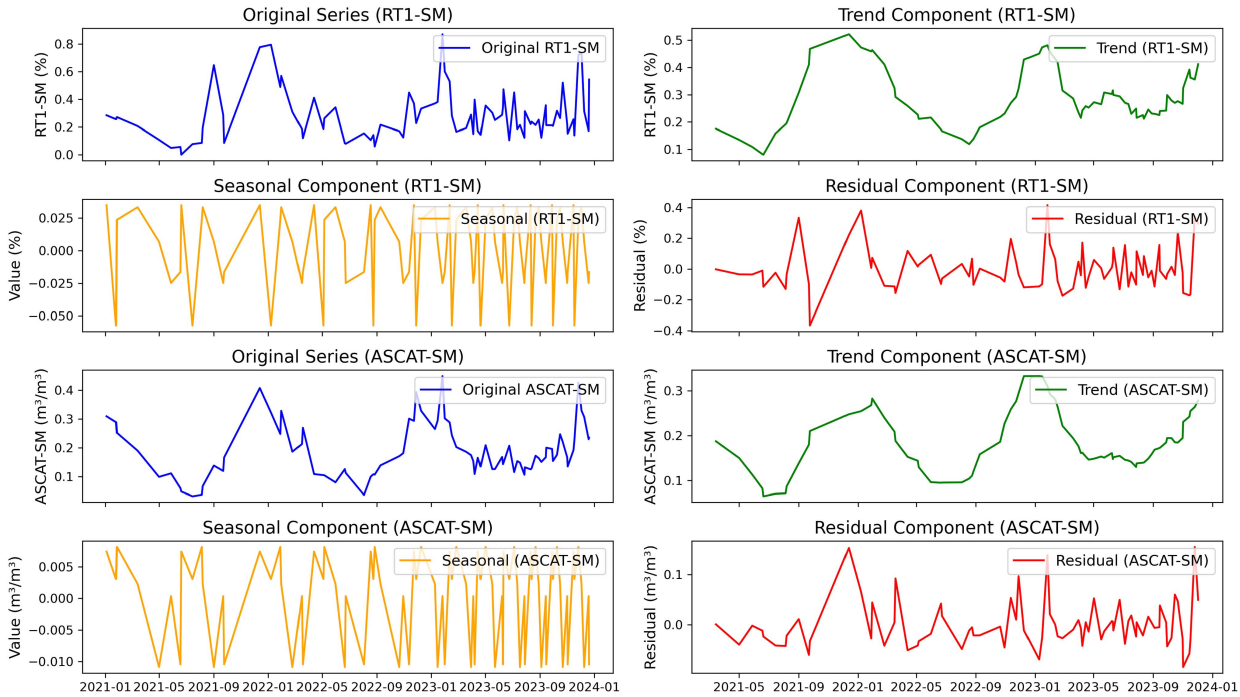

Fig. 12. Seasonality decomposition of RT1-SM and ASCAT-SM [2021–2023].

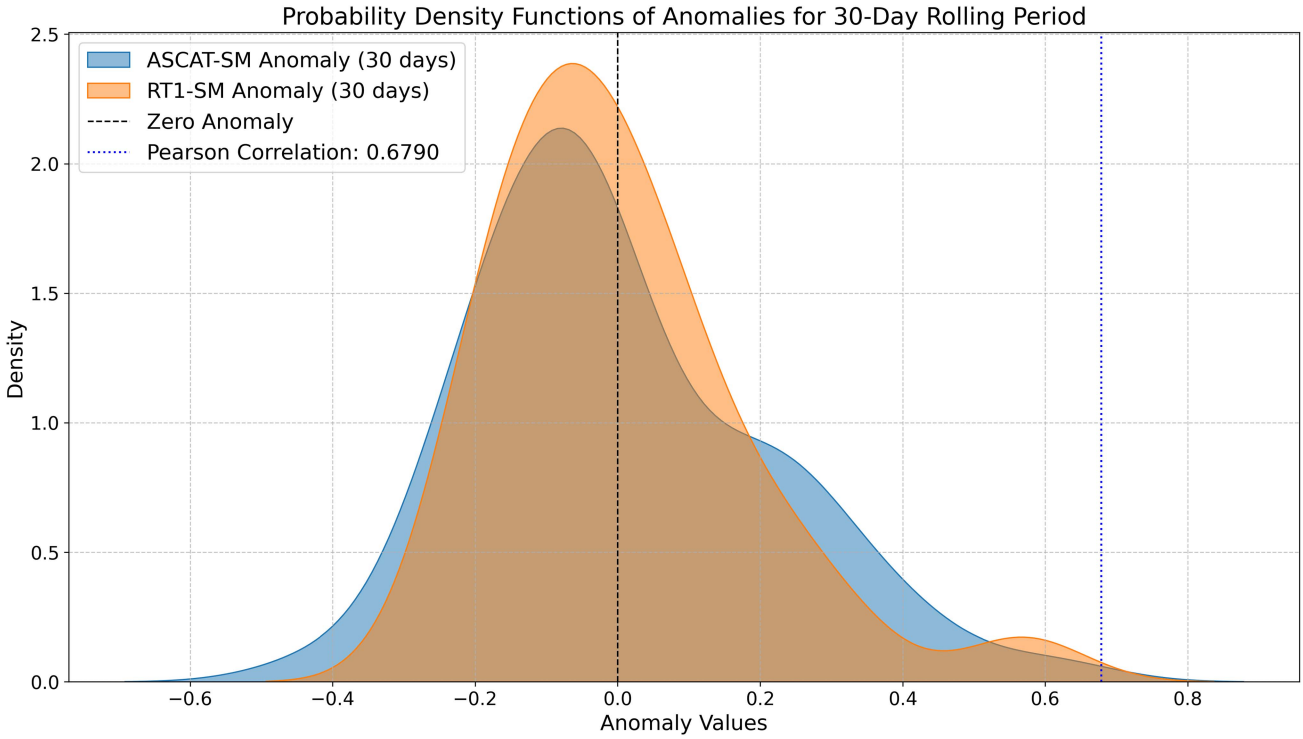

Fig. 13. Soil moisture anomalies (The blue shaded curve represents the PDF for ASCAT-SM anomalies, and the orange shaded curve represents the PDF for RT1-SM anomalies.

Overall, the backscatter exhibits clear seasonal patterns, with higher σ^0 values typically observed during wetter months—likely reflecting increased soil dielectric constant and vegetation water content. Conversely, lower backscatter values correspond to drier conditions, characterized by reduced soil moisture and sparse vegetation. Fig. 5 presents the time series of soil moisture retrievals, revealing distinct seasonal variations. Peak soil moisture values are typically observed during wetter months, while lower values are observed during the summer season, likely due to elevated temperatures and increased evapotranspiration.

TABLE III
SUMMARY OF PAIRWISE COMPARISONS AMONG SOIL MOISTURE DATASET (VOLUMETRIC UNITS, m^3/m^3)

Comparison	MSE	RMSE	Bias
SMAP-SM vs RT1-SM	0.0094	0.0968	-0.0400
ASCAT-SM vs RT1-SM	0.0088	0.0936	-0.0603
ERA5-swl1 vs RT1-SM	0.0097	0.0983	-0.0584
SMAP-SM vs ASCAT-SM	0.0057	0.0754	0.0125
SMAP-SM vs ERA5-swl1	0.0150	0.1225	-0.1107
ASCAT-SM vs ERA5-swl1	0.0225	0.1498	-0.1243

Although both ascending and descending orbital tracks exhibit similar temporal patterns, differences in magnitude may result from variations in surface conditions at the time of acquisition. The combined use of both orbit directions enhances temporal resolution and contributes to more reliable and continuous soil moisture monitoring.

The retrieved soil moisture estimates were rigorously validated against multiple independent reference datasets—including ASCAT, ERA5-Land, and SMAP—to ensure cross-sensor consistency and to evaluate model performance across varying spatial and temporal scales. Fig. 6 illustrates that during wet seasons (spring/summer), the RT1 retrievals show a stronger correlation with ASCAT and SMAP, particularly during periods of increased soil moisture. Seasonal patterns are apparent across all datasets, with ASCAT and SMAP displaying more pronounced variability than ERA5, which provides a smoother, less variable representation of soil moisture. Although RT1 retrievals are not continuous, they generally follow the seasonal patterns of the other datasets, particularly aligning with moisture peaks during wetter periods (October–November). While the RT1 retrievals effectively capture critical points within broader soil moisture trends, their lack of continuous temporal coverage makes them less suitable for comprehensive monitoring compared to the other datasets. Nevertheless, Fig. 6 illustrates the general consistency of the RT1 model with satellite observations and reanalysis data despite its limited temporal resolution. Brocca et al. [61] conducted a study to test and evaluate various soil moisture products in Italy, including those derived from Sentinel-1 datasets for the RT1 model. The findings revealed both the limitations and potential of the assessed products. Sentinel-1-based products, such as S1-COP and S1-RT1, demonstrated the ability to reproduce high-resolution spatial patterns, effectively detecting localized events related to irrigation, fire, and precipitation. Brunelli et al. [62] employed a change detection algorithm over the Po Valley in Italy using SAOCOM *L*-band data to map soil moisture beneath the vegetation layer. Their preliminary results demonstrated the potential of SAOCOM data for soil moisture retrieval under moderately vegetated conditions. However, in more complex environments—particularly those with dense vegetation cover—the change detection approach may be limited in its ability to fully represent vegetation structure and dynamics. In such cases, physically based models like RT1 offer a more comprehensive framework, as they account for bistatic scattering and decompose total backscatter into surface and volume contributions. The selection of an appropriate soil moisture retrieval model is application-specific. For instance, in densely vegetated regions such as the Petacciato landslide area, advanced radiative transfer modeling can provide a more accurate characterization of vegetation effects and thereby improve soil moisture estimation.

As LAI increases, particularly during spring and summer (refer to Fig. 7), the soil moisture values retrieved by the RT1 model become less variable. This is likely due to the canopy absorbing or scattering a substantial portion of the microwave signal, limiting the model's ability to detect changes in soil moisture. In addition, during these periods, soil moisture values may appear lower or less responsive because of interception by the vegetation, such as rainfall being absorbed by leaves. In contrast, during fall and winter, when LAI decreases, the RT1 model captures soil moisture fluctuations more clearly. With less vegetation, the microwave signal interacts more directly with the soil surface, improving the accuracy of soil moisture retrieval. This analysis underscores the importance of accounting for vegetation effects in radiative transfer models when estimating soil moisture in vegetated areas.

Fig. 8 illustrates the relationship between the API and RT1-SM, highlighting how the response of RT1 soil moisture to precipitation is influenced by various hydrological processes that unfold over time. Following a rainfall event, water must infiltrate the soil surface, saturate the upper layers, and gradually percolate downward, thereby affecting deeper soil moisture levels. In addition, processes such as evaporation and transpiration further complicate this relationship, as they can reduce moisture levels before the soil equilibrates with the newly added water. This observed delay underscores the importance of considering the temporal dynamics of soil moisture in response to precipitation, particularly when assessing potential impacts on hydrological behavior and slope stability, such as in landslide-prone areas. De Moraes et al. [79] describe the API as a method for estimating soil moisture. The study emphasizes the establishment of thresholds based on landslide occurrences to enhance the prediction of such events. The API demonstrates a linear relationship with soil moisture, making it a crucial parameter for landslide prediction and the development of early warning systems for mass movements. Zhao et al. [78] compared the predictive performance of RS thresholds with rainfall thresholds, finding that RS thresholds offer superior prediction capabilities characterized by higher hit rates and lower false alarm rates. These positive results suggest that the modified API provides improved performance in indexing soil moisture conditions, enhancing its utility for soil moisture estimation and related applications.

Fig. 9 illustrates that a lag of 0 indicates precipitation can immediately influence soil moisture levels. This immediate response is critical for understanding how initial rainfall saturates the upper soil layers, potentially triggering rapid changes in slope stability. Such saturation can increase pore pressure and reduce the soil's shear strength, thereby making slopes more vulnerable to failure and significantly heightening the risk of landslides. Conversely, a lag of 12 highlights the delayed effects of precipitation on soil moisture, indicating that significant changes in RT1-SM occur approximately 60 days after rainfall events. Understanding these temporal dynamics is critical for

managing the risk of slow-moving landslides, as it provides valuable insights for both immediate responses to rainfall and long-term monitoring strategies to ensure slope stability.

Figs. 10 and 11 illustrate that while RT1-SM shows a positive correlation with all datasets, the strength of the correlation varies. These variations are likely attributable to differences in how each dataset measures or represents soil moisture, such as differences in sensor type, spatial resolution, temporal resolution, or underlying model assumptions. Notably, RT1-SM exhibits a strong correlation with ASCAT data, while SMAP and ERA-5 also demonstrate significant intercorrelation.

The trend component of the seasonality decomposition, shown in Fig. 12, exhibits similar characteristics between datasets. However, RT1 demonstrates a more pronounced ability to capture seasonal cycles compared to the ASCAT data. Conversely, the residual components display comparable behavior, reflecting consistency in the representation of irregular variations.

Fig. 13 illustrates the PDFs of two sets of anomaly values over this period, with the blue-shaded area representing the PDF of ASCAT-SM Anomaly and the orange-shaded area corresponding to RT1-SM Anomaly. The shapes of the two distributions are quite similar, indicating that both ASCAT-SM and RT1-SM anomalies exhibit comparable behavior over time. Both PDFs peak near zero, meaning that for both datasets, most of the anomalies are small (close to their seasonal averages). The overlap between the two distributions is significant, showing that the anomalies from both datasets tend to fall within similar ranges. This suggests that both datasets capture variations in soil moisture in a similar way, which is expected given that both represent soil moisture conditions. The anomalies for both datasets range roughly between -0.6 and 0.4. This means that the deviations from the seasonal averages in both datasets can go below or above their mean values by up to about 0.6 and 0.4, respectively. A reported Pearson correlation coefficient of 0.67 suggests a moderate to strong positive linear relationship between the two dataset, implying that as anomalies in one dataset increase, those in the other dataset also tend to rise. Overall, the plot shows that both ASCAT-SM and RT1-SM anomalies have similar distributions and tend to follow similar patterns over time, as evidenced by the overlap in their PDFs.

The performance of RT1-derived soil moisture estimates was assessed through pairwise comparisons with satellite-based SMAP, ASCAT, and ERA5-swl1 datasets using standard error metrics: mean squared error (MSE), root mean squared error (RMSE), bias, and Peasrson's correlation. The comparison with ASCAT-SM yielded the lowest RMSE ($0.0936\ \mathrm{m}^3/\mathrm{m}^3$), lowest MSE (0.0088), and the highest correlation (0.6619), indicating that RT1 aligns more closely with active microwave observations. In contrast, comparisons with SMAP-SM and ERA5-swl1 resulted in slightly higher RMSE values (0.0968 and $0.0983\ \mathrm{m}^3/\mathrm{m}^3$, respectively) and moderate correlations (0.4312 and 0.4754), accompanied by systematic underestimation with biases of -0.0400 and $-0.0584\ \mathrm{m}^3/\mathrm{m}^3$, respectively. Notably, the intersensor comparisons among the reference datasets themselves (e.g., SMAP versus ERA5-swl1 and ASCAT versus ERA5-swl1) exhibited even larger discrepancies, with RMSE values up to $0.1498\ \mathrm{m}^3/\mathrm{m}^3$ and biases exceeding $-0.12\ \mathrm{m}^3/\mathrm{m}^3$. These results indicate that the RT1 retrievals fall within the expected range of interproduct variability and exhibit reliable performance, particularly in agreement with ASCAT. However, the consistent negative bias observed across all RT1 comparisons suggests a need for further refinement, potentially through improved parameterization strategy in future study.

Higher resolution soil moisture data (with spatial resolutions of tens of meters or finer) can significantly improve the understanding of how soil moisture variations influence relatively small-scale features, such as landslides. While landslides often measure only a few tens of meters in length and width, they can occasionally be much larger. Soil moisture exhibits considerable spatial variability even over small areas, driven by factors such as slope inclination and aspect, differences in material properties, and varying conditions of moisture recharge and drainage.

Liao et al. [63] emphasized the need for high-resolution spatial and temporal measurements of near-SSM in landslide-prone regions, employing airborne UAVSAR L-band data. The study applies a forward scattering model for soil moisture retrieval over grasslands. However, in this study, we focused on large-scale soil moisture variations due to the absence of in situ data for validation at finer spatial scales. Soil moisture dynamics are significantly influenced by complex topography, where factors such as slope, aspect, cultivation patterns, proximity to stream networks, land use land cover changes, and surface runoff play critical roles. In addition, the dense vegetation within the study area poses a challenge by attenuating microwave signals, thereby complicating soil moisture retrieval and potentially introducing inaccuracies. The absence of in situ sensors for validation further constrains the calibration and validation of SAR-derived results.

A primary limitation of the RT1 model is its restricted set of predefined BRDFs and volume-scattering phase functions, which currently includes only a few basic examples. Although future versions are expected to support more advanced scattering distributions, such as delta-peaked functions, these have not yet been implemented. In addition, when the number of expansion coefficients $(\mathrm{ncoefs} > 20)$ for BRDF or phase functions becomes large, the model may suffer from numerical precision errors, limiting its ability to accurately represent complex anisotropic scattering in heterogeneous surface conditions common to landslide-prone regions.

VI. Conclusion

This study represents the first evaluation of the RT1 modeling framework's capability to retrieve soil moisture using SAOCOM L-band SAR backscatter. It emphasizes the unique advantages of employing SAOCOM data and provides a comprehensive analysis of retrieval performance over a three-year period (2021–2023) in the absence of ground-truth measurements. The findings demonstrate a strong correlation with the ASCAT dataset, achieving a Pearson's correlation coefficient of 0.67, thereby underscoring the potential of resampled SAOCOM SAR backscatter σ^0 for soil moisture retrieval at a regional scale. In contrast, moderate correlations were found with the SMAP and ERA5 soil moisture datasets, while the API

exhibited a Pearson's correlation of 0.55. RT1 proves to be a flexible and adaptable approach that performs effectively in this application. In addition, the incorporation of rainfall data and the API enhances the robustness of the results, offering a more comprehensive approach to landslide risk assessment. This research offers new insights into soil moisture dynamics in landslide-prone areas, presenting a promising solution for improving landslide monitoring and reducing the impacts of these natural disasters on vulnerable communities.

To correct for effects induced by seasonal variability in the vegetation cover, the parametrization employs an LAI time series, scaled to a unified range to mimic the temporal signal of the associated vegetation optical depth (τ). The spatial variability of vegetation coverage was accounted for by retrieving a temporally constant estimate of the single-scattering albedo (ω). The assumption of a unified dynamic range for (τ), together with a spatially varying (ω), proved to be a robust method for correcting long-term vegetation dynamics with a minimal number of unknown variables.

This study reveals significant cross-correlation lags of 0 days and 12 days between the API and RT1-SM, which are critical for understanding slow-moving landslides. The 0-day lag indicates that rainfall can immediately affect soil moisture, leading to surface layer saturation that increases pore pressure and decreases soil shear strength, thereby heightening landslide risk. In contrast, the 12-day lag reveals that notable changes in RT1 SM occur roughly 12 days postrainfall, suggesting that moisture accumulation over time can further elevate the risk of slope instability in slow-moving landslides.

Seasonal variations in RT1 soil moisture were analyzed alongside ASCAT data, with both datasets exhibiting similar trends. However, RT1 captured seasonal cycles more distinctly than ASCAT. Residual components from both datasets displayed comparable patterns, reinforcing the reliability of the RT1 framework.

The proposed methodology represents a significant advancement in soil moisture retrieval, particularly for regional-scale landslide monitoring applications where in situ soil moisture data are often unavailable. By leveraging the enhanced vegetation penetration capabilities of L-band SAR and the novel RT1 radiative transfer model, this study improves the accuracy of soil moisture retrieval. The strong correlations between SAR-based soil moisture estimates and regional-scale datasets confirm the robustness of this approach, establishing it as a reliable tool for continuous soil moisture monitoring.

Future work will focus on achieving soil moisture retrieval at spatial resolutions ranging from 10 to 50 m, enabling detailed investigations into localized soil moisture dynamics and their impacts on small-scale geomorphic features such as landslides. This advancement is expected to provide a more precise understanding of the interactions between soil moisture and geomorphic processes.

To support these efforts, the planned installation of in situ sensors in landslide-prone regions will enable continuous monitoring of soil moisture. These sensors will deliver real-time data, providing valuable insights into soil moisture dynamics. Future research will also explore the feasibility of using this approach to retrieve high-resolution soil moisture data at a local scale, which is critical for understanding moisture variations that significantly influence slope stability and the occurrence of shallow landslides.

Moreover, obtaining high-resolution soil moisture data at spatial resolutions of 10–50 m will allow for a more detailed analysis of spatial variability, which is crucial for examining localized effects on slope stability. A sensitivity analysis will also be conducted to evaluate how different land cover types affect soil moisture retrieval at local scales. Soil moisture retrieval will be performed using multifrequency SAR datasets—Cosmo-SkyMed (X-band), Sentinel-1 (C-band), and SAOCOM (L-band)—to enable a more comprehensive comparison across frequencies. This analysis will provide insights into the influence of vegetation types and land use practices on soil moisture dynamics, enhancing the predictive capabilities for landslide risks and informing the development of effective mitigation strategies.

ACKNOWLEDGMENT

The authors would like to thank the Italian Space Agency (ASI) and CONAE for providing the SAOCOM datasets for my scientific research [57], the TU Wien Department of Geodesy and Geoinformation (Mr. Pavan Muguda Sanjeevamurthy) for supplying the ASCAT data and the necessary support. The processing and analysis of the results presented in this article were conducted using the RT1 Python package [48]. They also would like to thank to the various open-source packages that contributed to this work: NumPy [85], SciPy [76], and Pandas [86].

Credit authorship contribution statement: Divyeshkumar Rana: Data collection and processing, conceptualization, methodology, formal analysis, investigation, visualization, writing—Original draft. *Raphael Quast*: conceptualization, formal analysis, investigation, visualization, writing—review and editing. *Wolfgang Wagner*: Conceptualization, methodology, investigation, writing—review and editing, supervision. *Paolo Mazzanti*: Conceptualization, methodology, investigation, writing—review and editing, supervision. *Francesca Bozzano*: Investigation, writing—review and editing, supervision.

REFERENCES

[1] M. J. Froude and D. N. Petley, "Global fatal landslide occurrence from 2004 to 2016," *Natural Hazards Earth Syst. Sci.*, vol. 18, no. 8, pp. 2161–2181, 2018.

[2] D. Kirschbaum, T. Stanley, and Y. Zhou, "Spatial and temporal analysis of a global landslide catalog," *Geomorphology*, vol. 249, pp. 4–15, 2015.

[3] L. Brocca, F. Ponziani, T. Moramarco, F. Melone, N. Berni, and W. Wagner, "Improving landslide forecasting using ASCAT-derived soil moisture data: A case study of the torgiovannetto landslide in central Italy," *Remote Sens.*, vol. 4, no. 5, pp. 1232–1244, 2012.

[4] D. Rana, P. Mazzanti, and F. Bozzano, "Estimation of high-resolution soil moisture from dual frequency synthetic aperture radar (SAOCOM L-band & sentinel-1 C-band) dataset in the petacciato landslide area, Italy," in *Proc. 15th Eur. Conf. Synthetic Aperture Radar*, 2024, pp. 387–392.

[5] R. M. Iverson, "Landslide triggering by rain infiltration," *Water Resour. Res.*, vol. 36, no. 7, pp. 1897–1910, 2000.

[6] T. A. Bogaard and R. Greco, "Landslide hydrology: From hydrology to pore pressure," *Wiley Interdiscipl. Reviews: Water*, vol. 3, no. 3, pp. 439–459, 2016.

[7] D. Rana, P. Mazzanti, and F. Bozzano, "Assessing the correlation of time-series soil moisture and ground deformation at petacciato landslide,

Italy," *EGU General Assem. 2024*, Vienna, Austria, Apr. 14-19, 2024, doi: 10.5194/egusphere-egu24-912.
[8] M. Berti and A. Simoni, "Field evidence of pore pressure diffusion in clayey soils prone to landsliding," *J. Geophysical Res.: Earth Surf.*, vol. 115, no. F3, 2010.
[9] K. Terzaghi, "Mechanism of landslides," *Appl. Geology Eng. Practice*, Sidney Paige, 1950.
[10] S. L. Gariano and F. Guzzetti, "Landslides in a changing climate," *Earth-Sci. Rev.*, vol. 162, pp. 227–252, 2016.
[11] P. Lacroix, A. L. Handwerger, and G. Bièvre, "Life and death of slow-moving landslides," *Nature Rev. Earth Environ.*, vol. 1, no. 8, pp. 404–419, 2020.
[12] A. L. Handwerger, E. J. Fielding, M.-H. Huang, G. L. Bennett, C. Liang, and W. H. Schulz, "Widespread initiation, reactivation, and acceleration of landslides in the northern california coast ranges due to extreme rainfall," *J. Geophys. Research: Earth Surf.*, vol. 124, no. 7, pp. 1782–1797, 2019.
[13] W. H. Schulz, J. B. Smith, G. Wang, Y. Jiang, and J. J. Roering, "Clayey landslide initiation and acceleration strongly modulated by soil swelling," *Geophys. Res. Lett.*, vol. 45, no. 4, pp. 1888–1896, 2018.
[14] S.-B. Kim, M. Moghaddam, L. Tsang, M. Burgin, X. Xu, and E. G. Njoku, "Models of L-band radar backscattering coefficients over global terrain for soil moisture retrieval," *IEEE Trans. Geosci. Remote Sens.*, vol. 52, no. 2, pp. 1381–1396, Feb. 2014.
[15] W. Wagner et al., "Operational readiness of microwave remote sensing of soil moisture for hydrologic applications," *Hydrol. Res.*, vol. 38, no. 1, pp. 1–20, 2007.
[16] M. Zribi et al., "Analysis of L-band SAR data for soil moisture estimations over agricultural areas in the tropics," *Remote Sens.*, vol. 11, no. 9, 2019, Art. no. 1122.
[17] F. T. Ulaby, R. K. Moore, and A. K. Fung, *Microwave Remote Sensing: Active and Passive. Volume 3-From Theory to Applications*. Dedham, MA, USA: Artech House, 1986.
[18] Y. H. Kerr, P. Waldteufel, J.-P. Wigneron, J. Martinuzzi, J. Font, and M. Berger, "Soil moisture retrieval from space: The soil moisture and ocean salinity (SMOS) mission," *IEEE Trans. Geosci. Remote Sens.*, vol. 39, no. 8, pp. 1729–1735, Aug. 2001.
[19] D. Entekhabi et al., "The soil moisture active passive (SMAP) mission," *Proc. IEEE*, vol. 98, no. 5, pp. 704–716, May 2010.
[20] W. Wagner et al., "The ascat soil moisture product: A review of its specifications, validation results, and emerging applications," *Meteorologische Zeitschrift*, vol. 22, pp. 5–33, 2013, doi: 10.1127/0941-2948/2013/0399.
[21] J. Peng et al., "A roadmap for high-resolution satellite soil moisture applications–confronting product characteristics with user requirements," *Remote Sens. Environ.*, vol. 252, 2021, Art. no. 112162.
[22] A. Balenzano et al., "Sentinel-1 soil moisture at 1km resolution: A validation study," *Remote Sens. Environ.*, vol. 263, 2021, Art. no. 112554.
[23] B. Bauer-Marschallinger et al., "Toward global soil moisture monitoring with sentinel-1: Harnessing assets and overcoming obstacles," *IEEE Trans. Geosci. Remote Sens.*, vol. 57, no. 1, pp. 520–539, Jan. 2019.
[24] H. H. Nguyen, S. Cho, J. Jeong, and M. Choi, "A D-vine copula quantile regression approach for soil moisture retrieval from dual polarimetric sar sentinel-1 over vegetated terrains," *Remote Sens. Environ.*, vol. 255, 2021, Art. no. 112283.
[25] H.-J. F. Benninga, R. van der Velde, and Z. Su, "Sentinel-1 soil moisture content and its uncertainty over sparsely vegetated fields," *J. Hydrol. X*, vol. 9, 2020, Art. no. 100066.
[26] L. Zhu, R. Si, X. Shen, and J. P. Walker, "An advanced change detection method for time-series soil moisture retrieval from sentinel-1," *Remote Sens. Environ.*, vol. 279, 2022, Art. no. 113137.
[27] D. Mengen, T. Jagdhuber, A. Balenzano, F. Mattia, H. Vereecken, and C. Montzka, "High spatial and temporal soil moisture retrieval in agricultural areas using multi-orbit and vegetation adapted sentinel-1 SAR time series," *Remote Sens.*, vol. 15, no. 9, 2023, Art. no. 2282.
[28] N. Bhogapurapu, S. Dey, A. Bhattacharya, C. López-Martínez, I. Hajnsek, and Y. S. Rao, "Soil permittivity estimation over croplands using full and compact polarimetric SAR data," *IEEE Trans. Geosci. Remote Sens.*, vol. 60, 2022, Art. no. 4415917.
[29] L. Zhuo, Q. Dai, D. Han, N. Chen, B. Zhao, and M. Berti, "Evaluation of remotely sensed soil moisture for landslide hazard assessment," *IEEE J. Sel. Topics Appl. Earth Observ. Remote Sens.*, vol. 12, no. 1, pp. 162–173, Jan. 2019.
[30] I. Hajnsek, T. Jagdhuber, H. Schon, and K. P. Papathanassiou, "Potential of estimating soil moisture under vegetation cover by means of polSAR," *IEEE Trans. Geosci. Remote Sens.*, vol. 47, no. 2, pp. 442–454, Feb. 2009.
[31] M. Hosseini and H. McNairn, "Using multi-polarization C-and L-band synthetic aperture radar to estimate biomass and soil moisture of wheat fields," *Int. J. Appl. Earth Observation Geoinformation*, vol. 58, pp. 50–64, 2017.
[32] H. Ma et al., "An assessment of l-band surface soil moisture products from SMOS and SMAP in the tropical areas," *Remote Sens. Environ.*, vol. 284, 2023, Art. no. 113344s.
[33] Y. Xu, J. Kim, D. L. George, and Z. Lu, "Characterizing seasonally rainfall-driven movement of a translational landslide using SAR imagery and SMAP soil moisture," *Remote Sens.*, vol. 11, no. 20, 2019, Art. no. 2347.
[34] H. Dadkhah, D. Rana, E. Ghaderpour, and P. Mazzanti, "Integrating multi-sensor remote sensing data for comprehensive spatio-temporal wildfire-assessment in campania provinces– Italy," in *Proc. Copernicus Meetings*, 2024.
[35] Q. Gao, M. Zribi, M. J. Escorihuela, and N. Baghdadi, "Synergetic use of sentinel-1 and sentinel-2 data for soil moisture mapping at 100m resolution," *Sensors*, vol. 17, no. 9, 2017, Art. no. 1966.
[36] H. Ma et al., "Surface soil moisture from combined active and passive microwave observations: Integrating ASCAT and SMAP observations based on machine learning approaches," *Remote Sens. Environ.*, vol. 308, 2024, Art. no. 114197.
[37] O. Merlin, C. Rudiger, A. Al Bitar, P. Richaume, J. P. Walker, and Y. H. Kerr, "Disaggregation of SMOS soil moisture in southeastern Australia," *IEEE Trans. Geosci. Remote Sens.*, vol. 50, no. 5, pp. 1556–1571, May 2012.
[38] S. Paloscia, S. Pettinato, E. Santi, C. Notarnicola, L. Pasolli, and A. Reppucci, "Soil moisture mapping using sentinel-1 images: Algorithm and preliminary validation," *Remote Sens. Environ.*, vol. 134, pp. 234–248, 2013.
[39] M. Foucras, M. Zribi, C. Albergel, N. Baghdadi, J.-C. Calvet, and T. Pellarin, "Estimating 500-m resolution soil moisture using sentinel-1 and optical data synergy," *Water*, vol. 12, no. 3, 2020, Art. no. 866.
[40] M. El Hajj, N. Baghdadi, and M. Zribi, "Comparative analysis of the accuracy of surface soil moisture estimation from the C-band L-bands," *Int. J. Appl. Earth Observation Geoinformation*, vol. 82, 2019, Art. no. 101888.
[41] E. Ghaderpour, H. Dadkhah, H. Dabiri, F. Bozzano, G. Scarascia Mugnozza, and P. Mazzanti, "Precipitation time series analysis and forecasting for italian regions," *Engi. Proc.*, vol. 39, no. 1, 2023, Art. no. 23.
[42] H. Dadkhah, D. Rana, E. Ghaderpour, M. Ferrarotti, and P. Mazzanti, "Multi-sensor approach to assessing the wildfire severity-induced landslide risk: A case of ischia island, Italy," in *Proc. IEEE Int. Geosci. Remote Sens. Symp.*, 2024, pp. 3448–3452.
[43] A. Graham and R. Harris, "Extracting biophysical parameters from remotely sensed radar data: A review of the water cloud model," *Prog. Phys. Geogr.*, vol. 27, no. 2, pp. 217–229, 2003.
[44] A. Wicki, P. Lehmann, C. Hauck, S. I. Seneviratne, P. Waldner, and M. Stähli, "Assessing the potential of soil moisture measurements for regional landslide early warning," *Landslides*, vol. 17, pp. 1881–1896, 2020.
[45] T. Jagdhuber, I. Hajnsek, K. P. Papathanassiou, and A. Bronstert, "Soil moisture retrieval under agricultural vegetation using fully polarimetric SAR," in *Proc. IEEE Int. Geosci. Remote Sens. Symp.*, 2012, pp. 1481–1484.
[46] R. Quast, W. Wagner, B. Bauer-Marschallinger, and M. Vreugdenhil, "Soil moisture retrieval from sentinel-1 using a first-order radiative transfer model—A case-study over the Po-valley," *Remote Sens. Environ.*, vol. 295, 2023, Art. no. 113651.
[47] R. Quast, C. Albergel, J.-C. Calvet, and W. Wagner, "A generic first-order radiative transfer modelling approach for the inversion of soil and vegetation parameters from scatterometer observations," *Remote Sens.*, vol. 11, no. 3, 2019, Art. no. 285.
[48] R. Quast, "RT1," 2021. [Online]. Available: https://rt1.readthedocs.io/en/latest/
[49] R. Quast and W. Wagner, "Analytical solution for first-order scattering in bistatic radiative transfer interaction problems of layered media," *Appl. Opt.*, vol. 55, no. 20, pp. 5379–5386, 2016.
[50] S. Lignon, F. Laouafa, F. Prunier, H. D. V. Khoa, and F. Darve, "Hydro-mechanical modelling of landslides with a material instability criterion," *Geotechnique*, vol. 59, no. 6, pp. 513–524, 2009.
[51] C. R. Group, "Geotechnical report for Petacciato landlside," Sapienza Univ. Rome, Rome, Italy, Tech. Rep., 2022.
[52] F. Fiorillo, "Geological features and landslide mechanisms of an unstable coastal slope (Petacciato, Italy)," *Eng. Geol.*, vol. 67, no. 3/4, pp. 255–267, 2003.

[53] M. Fiorucci, S. Martino, M. Della Seta, L. Lenti, and A. Mancini, "Seismic response of landslides to natural and man-induced ground vibrations: Evidence from the petacciato coastal slope (central Italy)," *Eng. Geol.*, vol. 309, 2022, Art. no. 106826.
[54] M. Fiorucci et al., "Long-term hydrological monitoring of soils in the terraced environment of cinque terre (North-Western Italy)," *Front. Earth Sci.*, vol. 11, 2023, Art. no. 1285669.
[55] S. Tarquini and L. Nannipieri, "The 10 m-resolution tinitaly DEM as a trans-disciplinary basis for the analysis of the italian territory: Current trends and new perspectives," *Geomorphology*, vol. 281, pp. 108–115, 2017.
[56] S. Tarquini, S. Vinci, M. Favalli, F. Doumaz, A. Fornaciai, and L. Nannipieri, "Release of a 10-m-resolution DEM for the italian territory: Comparison with global-coverage DEMs and anaglyph-mode exploration via the web," *Comput. Geosci.*, vol. 38, no. 1, pp. 168–170, 2012.
[57] ASI, "Satélite argentino de observación con microondas (argentine microwaves observation satellite)," 2020. [Online]. Available: https://www.asi.it/en/earth-science/saocom/
[58] ECMWF, "Era5-land hourly data from 1950 to present," 2019. [Online]. Available: https://cds.climate.copernicus.eu/cdsapp#!/dataset/reanalysis-era5-land?tab=overview
[59] J. Muñoz-Sabater et al., "Era5-land: A state-of-the-art global reanalysis dataset for land applications," *Earth Syst. Sci. Data*, vol. 13, no. 9, pp. 4349–4383, 2021.
[60] Google and NSIDC, "Spl4smgp.007 smap l4 global 3-hourly 9-km surface and root zone soil moisture," 2015. [Online]. Available: https://developers.google.com/earth-engine/datasets/catalog/NASA_SMAP_SPL4SMGP_007#description
[61] L. Brocca et al., "Exploring the actual spatial resolution of 1km satellite soil moisture products," *Sci. Total Environ.*, vol. 945, 2024, Art. no. 174087.
[62] B. Brunelli, D. Festa, F. Mancini, and W. Wagner, "Surface soil moisture retrieval via change detection using SAOCOM l-band data over the Po valley (Italy)," in *Proc. EGU Gen. Assem. Conf. Abstr.*, 2024, Art. no. 16418.
[63] T.-H. Liao, S.-B. Kim, A. L. Handwerger, E. J. Fielding, M. H. Cosh, and W. H. Schulz, "High-resolution soil-moisture maps over landslide regions in northern california grassland derived from SAR backscattering coefficients," *IEEE J. Sel. Topics Appl. Earth Observ. Remote Sens.*, vol. 14, pp. 4547–4560, 2021.
[64] W. Wagner et al., "The ascat soil moisture product: A review of its specifications, validation results, and emerging applications," *Meteorologische Zeitschrift*, vol. 22, no. 1, pp. 5–33, 2013. [Online]. Available: http://dx.doi.org/10.1127/0941?2948/2013/0399
[65] E. Hsaf, "Eumetsat HSAF ASCAT soil moisture," 2007. [Online]. Available: http://www.ipf.tuwien.ac.at/radar
[66] C. Funk et al., "The climate hazards infrared precipitation with stations—A new environmental record for monitoring extremes," *Sci. Data*, vol. 2, no. 1, pp. 1–21, 2015.
[67] P. C. Dubois, J. Van Zyl, and T. Engman, "Measuring soil moisture with imaging radars," *IEEE Trans. Geosci. Remote Sens.*, vol. 33, no. 4, pp. 915–926, Jul. 1995.
[68] Y. Oh, "Quantitative retrieval of soil moisture content and surface roughness from multipolarized radar observations of bare soil surfaces," *IEEE Trans. Geosci. Remote Sens.*, vol. 42, no. 3, pp. 596–601, Mar. 2004.
[69] N. Baghdadi and M. Zribi, "Evaluation of radar backscatter models IEM, oh and dubois using experimental observations," *Int. J. Remote Sens.*, vol. 27, no. 18, pp. 3831–3852, 2006.
[70] J. L. Álvarez-Pérez, "An extension of the IEM/IEMM surface scattering model," *Waves Random Media*, vol. 11, no. 3, 2001, Art. no. 307.
[71] J. L. Alvarez-Pérez, "The IEM2M rough-surface scattering model for complex-permittivity scattering media," *Waves Random Complex Media*, vol. 22, no. 2, pp. 207–233, 2012.
[72] K.-L. Chen, K.-S. Chen, Z.-L. Li, and Y. Liu, "Extension and validation of an advanced integral equation model for bistatic scattering from rough surfaces," *Prog. Electromagnetics Res.*, vol. 152, pp. 59–76, 2015.
[73] R. Fieuzal and F. Baup, "Improvement of bare soil semi-empirical radar backscattering models (oh and dubois) with SAR multi-spectral satellite data (x-, c-and l-bands)," *Adv. Remote Sens.*, vol. 5, no. 4, pp. 296–314, 2016.
[74] P. de Matthaeis and R. Lang, "Microwave scattering models for cylindrical vegetation components," *Prog. Electromagnetics Res.*, vol. 55, pp. 307–333, 2005.
[75] J. Moré, "Numerical Analysis the Levenberg-Marquardt Algorithm: Implementation and Theory," Berlin, Germany: Springer, 1978.
[76] P. Virtanen et al., "Scipy 1.0: Fundamental algorithms for scientific computing in python," *Nature methods*, vol. 17, no. 3, pp. 261–272, 2020.
[77] A. Nanda, N. Das, G. Singh, R. Bindlish, K. M. Andreadis, and S. Jayasinghe, "Harnessing SMAP satellite soil moisture product to optimize soil properties to improve water resource management for agriculture," *Agricultural Water Manage.*, vol. 300, 2024, Art. no. 108918.
[78] B. Zhao et al., "Estimation of soil moisture using modified antecedent precipitation index with application in landslide predictions," *Landslides*, vol. 16, pp. 2381–2393, 2019.
[79] M. A. E. D. Moraes et al., "Antecedent precipitation index to estimate soil moisture and correlate as a triggering process in the occurrence of landslides," *Int. J. Geosciences*, vol. 15, no. 1, pp. 70–86, 2024.
[80] S. Ali, N. Ghosh, and R. Singh, "Rainfall–runoff simulation using a normalized antecedent precipitation index," *Hydrological Sci. J.–J. des Sci.* Hydrologiques, vol. 55, no. 2, pp. 266–274, 2010.
[81] R. J. Heggen, "Normalized antecedent precipitation index," *J. Hydrologic Eng.*, vol. 6, no. 5, pp. 377–381, 2001.
[82] M. A. Kohler and R. K. Linsley, *Predicting the Runoff From Storm Rainfall*. College Park, MD, USA: U.S. Dept. Commerce, 1951.
[83] V. P. Singh and D. K. Frevert, "Watershed modeling," in *Proc. World Water Environ. Resour. Congr.*, 2003, pp. 1–37.
[84] F. Meyer, "Spaceborne synthetic aperture radar: Princ., data access, and basic process. techn.," in *Synthetic Aperture Radar (SAR) Handbook: Comprehensive Methodologies Forest Monitoring Biomass Estimation*. 2019, pp. 21–64, doi: 10.25966/nr2c-s697.
[85] C. R. Harris et al., "Array programming with NumPy," *Nature*, vol. 585, no. 7825, pp. 357–362, 2020.
[86] W. McKinney et al., "Data structures for statistical computing in python," *SciPy*, vol. 445, no. 1, pp. 51–56, 2010.
[87] D. Entekhabi, R. H. Reichle, R. D. Koster, and W. T. Crow, "Performance metrics for soil moisture retrievals and application requirements," *J. Hydrometeorol.*, vol. 11, no. 3, pp. 832–840, 2010.
[88] D. Hillel, *Environmental Soil Physics*. San Diego, CA, USA: Academic, 1998.

Divyeshkumar Rana (Student Member, IEEE) received the bachelor's degree in civil engineering from Dr. S. and S. S. Gandhi Government Engineering College, Surat, India, in 2018, and the master's degree in geomatics from CEPT University, Ahmedabad, India, in 2020. He is currently working toward the National Ph.D. degree in Earth observation with the Department of Earth Sciences, Sapienza University of Rome, Rome, Italy, under the guidance of Prof. Paolo Mazzanti and Prof. Francesca Bozzano. His Ph.D. dissertation was titled "Multi-Frequency SAR Datasets for Ground Deformation and Soil Moisture Monitoring of Unstable Ground," aims to explore the relationship between soil moisture and ground deformation caused by landslides, sinkholes, and subsidence.

An enthusiastic and quick learner with a strong interest in innovation and technology, he is passionate about remote sensing sciences. His research focuses on multifrequency SAR datasets for soil moisture retrieval using the radiative transfer algorithm (RT1) and applies PS-InSAR techniques to monitor ground deformation associated with landslides, sinkholes, and subsidence.

Dr. Rana is also an active member of IEEE Geoscience and Remote Sensing Society Standards Committee, IEEE Remote sensing Environment, Analysis and Climate Technologies Technical Committee, and the Indian Society of Geomatics (ISG) in India.

Raphael Quast is currently working toward the Ph.D. degree in microwave remote sensing with the Vienna University of Technology, Vienna, Austria, and is affiliated with GeoSphere Austria, Vienna, Austria.

Wolfgang Wagner (Senior Member, IEEE) received the Dipl.-Ing. degree in physics and the Dr.techn. degree in remote sensing from Vienna University of Technology (TU Wien), Vienna, Austria, in 1995 and 1999, respectively.

From 1999 to 2001, he was with DLR, Oberpfaffenhofen, Germany. In 2001, he was a Professor for Remote Sensing with TU Wien. He is a Co-Founder of the Earth Observation Data Centre (EODC), Vienna, Austria. He has developed models for retrieving soil moisture and other land surface variables from a scatterometer, synthetic aperture radar (SAR), and full-waveform LiDAR observations. His main research interest is to gain a physical understanding of the mechanisms driving the interaction of electromagnetic waves with the land surface.

Dr. Wagner is a member of the advisory groups for METOP-SG SCA, Sentinel-1 NG, and HydroGNSS. In support of his master's and Ph.D. studies, he was the recipient of fellowships to carry out research at NASA, ESA, and the EC Joint Research Centre. He was also the recipient of the ISPRS Frederick J. Doyle Award and the Friedrich Hopfner Medal awarded by the Austrian Geodetic Commission. From 2008 to 2012, he was the ISPRS Commission VII President; from 2009 to 2011, he was an Editor-in-Chief of the open-access journal *Remote Sensing*, and from 2016 to 2019, he was the Chair for the GCOS/WCRP Terrestrial Observation Panel for Climate.

Paolo Mazzanti received the Graduate degree in geology and the Ph.D. degree in earth sciences.

He is currently a Professor of Engineering Geology and a Lecturer on Remote Sensing and Geological Risks with the Department of Earth Sciences, Sapienza University of Rome, Rome, Italy, the largest university in Europe, and a member of Centro di Ricerca per la Previsione, Prevenzione e Controllo dei Rischi Geologici (CERI), Rome, Italy. He is also the Co-Founder of NHAZCA S.r.l., a startup of Sapienza University of Rome. He organizes professional training courses in Italy and abroad, including the annual "International Course on Geotechnical and Structural Monitoring," which has attracted more than 650 professionals from 50+ countries and 40 renowned partners. With more than 35 supervised degrees and doctoral theses in Engineering Geology, Geotechnics, and Remote Sensing, he has also been an invited speaker at universities and research centers worldwide. He serves on various technical committees, including the TRB Engineering Geology Committee, the International Society of Soil Mechanics and Geotechnical Engineering, and PIARC, and audits for AIGA. Over the last 15 years, he has managed technical consulting projects in tunnels, oil and gas, dams, transport infrastructures, landslides, and archaeological assets in 15+ countries. He has authored 120+ scientific papers on applied geology, remote sensing, geotechnical and structural monitoring, radar monitoring systems, and infrastructure management.

Francesca Bozzano received the Graduate degree in geological sciences from the University of Rome "La Sapienza," Rome, Italy, in 1987 and the Ph.D. degree in earth sciences.

From 1991 to 2000, a Researcher from the University of Rome "La Sapienza," an Associate Professor from November 2000 to November 2013 and then a Full Professor with the Department of Earth Sciences, Engineering Geology "Sapienza" University of Rome, Rome, Italy. Since 2003, she has been a member of the CERI Research Centre (Prediction, Prevention and Mitigation of Geological Risks), Rome, Italy. Since 2009, she has been a partner of NHAZCA, Rome, Italy, a spin-off company of the "Sapienza" University of Rome," Rome, Italy. She was a member of the Technical Secretariat, Italian Ministry of Environment, Land and Sea Protection (Directorate-General: Quality of Life) from 2010 to 2013. She was also a Director of the CERI Research Centre (Prediction, Prevention and Mitigation of Geological Risks), "Sapienza" University of Rome, from August 2014 to October 2020. Her research interests include landslides, triggered by rainfall and earthquakes, subsidence, Sinkholes in urban areas, multigeological hazards and risks, land, structures and infrastructures monitoring, prediction of the evolution of geological instabilities processes and engineering geological design of structures, infrastructures and remedial interventions.

Dr. Bozzano was a member of the Italian Major Risk National Committee (meteo-hydrogeological, hydraulic and landslide risk sector) appointed by the Prime Ministerial Decree for the period 2017–2023 and by the Minister for Civil Protection and Sea Policies for the period 2023–2028. Since December 2017 Member of the board of directors of the INGV (Istituto Nazionale di Geofisica e Vulcanologia) appointed by the Minister of the Education, University and Research. Since January 2021, she has been serving a Deputy Rector for "Relation with research centers and bodies, consortia and association for the third mission."